Low-Thrust Spacecraft Maneuver Determination Without Time/Magnitude Knowledge

Aitor R. Gomez*
Aalborg University, 9220 Aalborg, Denmark
and
Christopher K. Nebelecky† and John L. Crassidis‡
University at Buffalo, State University of New York, Amherst, New York 14260-4400

The detection and estimation of spacecraft maneuvers, when the effects of that maneuver are not seen until after it occurs, are critical to ensuring the safety and efficacy of space traffic management and domain awareness. In this study, a new method is shown to determine the time, direction, and magnitude of small impulsive spacecraft maneuvers using a sequence of ground observations. The approach combines adaptive estimation techniques with relative linear models to provide recursive maneuver estimations. The nominal state of the spacecraft is perturbed and propagated forward in a particle-like filter manner, based on multiple-model adaptive estimation, using different assumed maneuvers until the time of each new observation. Maximum likelihood is used to provide an estimate of the time of the actual maneuver and enables subsequent estimation of the direction and magnitude of the maneuver. The forward propagation is enabled by state transition matrices, which allow the efficient propagation of large numbers of particles. The results are demonstrated for two different cases: a near-Earth case where Keplerian concepts can reduce computations by leveraging closed-form solutions and a general case presented through a cislunar scenario. The results demonstrate the effectiveness of the proposed method in the presence of measurement noise and process uncertainties and show potential for applications in both spacecraft operations and space domain awareness.

Nomenclature

A	=	Jacobian of the equations of motion
C	=	state error covariance
E	=	expectation operator
$e_{i,j}^-$	=	residual measurement vector based on jth maneuver and ith time of execution
$\mathcal{E}_{i,j}^-$	=	measurement covariance based on jth maneuver and ith time of execution
f	=	drift function or deterministic vector field
G	=	process noise covariance
g	=	gravity model
H	=	Jacobian of the measurement function
h	=	measurement function
i	=	time index
j	=	maneuver index
M	=	number of particles in the MMAE procedure
P	=	discrete probability measure
Q_k	=	measurement white noise
R	=	measurement noise covariance
$r_n, \dot{r}_n$	=	nominal/unperturbed position and velocity vectors in the ECI frame
$r, \dot{r}$	=	position and velocity vectors in the ECI frame
$r', \dot{r}'$	=	position and velocity vectors in the synodic frame
$T_{\Delta t_s}$	=	set of discretized times
t_m	=	time of execution of the maneuver
(W_t)	=	Wiener process
X	=	random state variable
(X_t)	=	stochastic process
x_n	=	nominal/unperturbed state vector
x	=	state vector
$\hat{x}$	=	estimated state vector
$\hat{x}_{i,j}^-$	=	estimated state vector based on jth maneuver and ith time of execution
Y_k	=	noisy measurement variable
$\mathcal{Y}_k$	=	set of observation vectors
y	=	measurement vector, m
$\hat{y}_{i,j}^-$	=	estimated measurement vector based on jth maneuver and ith time of execution, m
Δt	=	increment of time, s
Δt_s	=	increment of time in the MMAE procedure, s
ΔV	=	instantaneous change in velocity vector, m/s
δx	=	relative state vector with respect to nominal/unperturbed state
$\mu_\oplus, \mu_\ominus$	=	Earth's and moon's gravitational constants, respectively, m³/s²
$\tilde{\Theta}$	=	compact set of available maneuvers
Θ_M	=	finite family of maneuvers defining the searching space
θ	=	maneuver vector defined as an instantaneous change in velocity for the MMAE procedure, m/s
$\hat{\theta}$	=	estimator of the maneuver vector, m/s
$\theta_{\min}, \theta_{\max}$	=	minimum and maximum values bounding the maneuver search space, m/s
Ξ	=	Jacobian of the dynamics with respect to positional coordinates
$\rho, \dot{\rho}$	=	relative position and velocity vector with respect to nominal position vector
Σ	=	diffusion matrix
τ_j	=	discrete time between t_0 and t_1 defined for the MMAE procedure, s
$\hat{\tau}$	=	estimator of the maneuver execution time, s
Φ	=	state transition matrix
χ	=	sigma point vector
Ω	=	angular velocity vector, rad/s

*Ph.D. Student, Department of Electronic Systems, Automation & Control Section; arg@es.aau.dk.
†Research Scientist, Department of Mechanical & Aerospace Engineering; ckn@buffalo.edu.
‡SUNY Distinguished Professor and Moog Endowed Chaired Professor of Innovation, Department of Mechanical & Aerospace Engineering; johnc@buffalo.edu. Fellow AIAA.

I. Introduction

AS THE space environment becomes increasingly congested and contested, the importance of space domain awareness (SDA) continues to grow. SDA is the ability of building effective knowledge to understand and predict the evolution of objects in space—particularly, but not exclusively, near Earth where valuable human-made objects reside. The aim of SDA is to provide the necessary information to perform critically reasoned decisions to enhance the overall safety of the space environment. A wide variety of techniques and technologies, such as ground- and space-based sensors, modeling, simulation, and data analysis, are used to achieve SDA.

One fundamental component of SDA is identifying and tracking space objects based on observational data collected by a variety of sensors. The process of matching observations of space objects to their respective tracks, generally referred to as data association (DA), is challenging [1]. The difficulty of performing DA resides in several aspects. For example, multiple sensors make observations of the objects to obtain an accurate characterization of their orbit and motion. These observations might be taken at different times and from different angles, making the gathered data of one same object difficult to correlate [2]. Also, the space environment is constantly changing; some spacecraft perform maneuvers to modify their orbits, merge with other objects, or split into multiple smaller ones. In this particular context, determination of spacecraft maneuvers becomes instrumental to obtain a more precise picture of the space environment and facilitate DA.

In addition, maneuvers are used for altitude, phase and trajectory corrections, and collision avoidance. They can also be indicators of intended activity that can potentially be threatening. Spacecraft malfunctions causing unintended orbital maneuvers are equally important from the standpoint of SDA, because such changes in orbit might lead to an increased risk of collision with other spacecraft and/or debris. Detecting and characterizing spacecraft maneuvers can, withal, predict the future trajectory of spacecraft, identify potential risks of collision, and reveal possible threatening activities. Maneuver determination (MD) is an important aspect of SDA with vast implications for space safety, surveillance, and space traffic management.

For such reasons, detecting and characterizing maneuvers is a well-studied problem in the literature. Among different studies, some common methodologies involve trajectory propagation, filtering, and statistical error modeling. Propagating a trajectory provides a way to link the gap between (presumably correlated) observations, which is essential for DA. Propagation is usually performed forward by means of statistical models and filters because there is special interest in characterizing the uncertainty of the predictions in real-time. Modifications of the classic extended Kalman filter (EKF) [3] are among the most appealing [4–6] due to the simplicity of the algorithm and its well-understood properties.

Spacecraft maneuvers, however, are sources of potential instability for the EKF when large unexpected differences between observations and predictions exist. Goff et al. [4] overcome this limitation by inflating the error covariance matrix propagated by an EKF once a maneuver has been detected so that the discrepancies in the prediction are bound by the uncertainty of the model. In that work, maneuvers are detected by monitoring a certain parameter defined from the residual between the observations and the predictions. This parameter initiates the inflation of the error covariance when it exceeds a predefined threshold and reduces the possibility of divergence of the algorithm. However, it can cause larger errors in the estimation of the maneuver. After a maneuver detection, Goff et al. and Jia et al. [4,5] use multiple-model adaptive estimation (MMAE) [3,7] strategies to converge to the new orbit. Maneuvers can be determined by approximating the acceleration due to thrust as a Fourier series and using a KF to estimate the coefficients [8]. In that work, a maneuver is declared when the norm of the Fourier coefficients exceeds a predefined threshold. Formulations based on optimization problems have also been explored, leveraging the insight that orbital maneuvers often optimize some metric such as fuel consumption or maneuver time. Assuming orbital in-track maneuvers only, Jian et al. [9] estimate the execution time of the maneuver and an instantaneous velocity change tangent to the orbital path. The problem is framed as a second-order cone programming by employing state transition matrices. More complex formulations are explored in [10], where the optimal path linking the observations is determined by solving a variational control problem. Optimal control policies and distance metrics with an accompanying maneuver detection algorithm that determines when the system's dynamics are mismodeled are shown in [11]. Escribano et al. [12] employ a stochastic hybrid system with a regularized particle filter, enhanced by a Markov chain Monte Carlo characterization for postmaneuver state hypotheses to detect a maneuver.

Another aspect of SDA is understanding the space operational picture that includes regularized-timed thrusting maneuvers and deviations from them. Regularized-timed thrusting maneuvers are used for a variety of reasons, including station-keeping for orbit maintenance, which are often done autonomously [13]. Deviations from these regular corrections may indicate that the spacecraft is performing nonbenign activities. Common approaches to enhance SDA for various types of maneuvers involve developing "patterns of life" (PoL), which mimic habits of a person or population. Most PoL approaches for characterizing the types of thrusting maneuvers are based on some form of artificial intelligence and machine learning (AI/ML). Several categories of AI/ML algorithms exist to support PoL development. Linear regression and decision trees are the simplest forms of AI/ML. These algorithms utilize labeled training data and can often be trained using data sets of modest size [14]. Neural networks [15] interpret numerical patterns that can take the shape of vectors. The main advantage of neural networks is that they can readily adapt to changing output patterns. However, neural networks typically require large volumes of training data. DiBona et al. [16] employ a "probabilistic assessment of space threats" approach that involves machine-learning approaches to both categorize the type of orbital maneuver and assess whether the maneuver is nominal or anomalous based on that spacecraft's PoL. Cipollone et al. [17] exploit a "long-short-term-memory" neural network, which can provide detection without any externally defined threshold or parameter tuning by operators. Various orbital elements are chosen to embed sensitivity to any kind of variation involved in the neural-network PoL. No matter the PoL approach employed, sufficient quantities of accurate training data are vital to their success.

All the aforementioned approaches for MD and for PoL analyses assume that the space objects are observed close to the maneuver time and/or do not estimate the actual maneuver magnitude. This work presents an approach that does not make the assumption that measurements are available during or close to the maneuver time. Specifically, the main goal is to accurately predict the time a maneuver has occurred well after it has happened, along with the magnitude and direction. All maneuvers are assumed to be performed by high-magnitude thrusters and burns lasting no more than several minutes. The total velocity change delivered by these types of (impulsive) maneuvers can be reasonably assumed to be instantaneous. Consequently, determining the instantaneous change in velocity vector, ΔV, is equivalent to determining the maneuver itself. Moreover, considering that spacecraft maneuvers are usually constrained by the spacecraft's specific impulse, the norm of the velocity change vector can be upper- and lower-bounded.

This work proposes a novel approach for MD that estimates the magnitude, direction, and time of execution. Inspired by the study of Kharti et al. [18], which primarily focuses on forward-filtering formulations, the strategy in this work leverages the advantages of linear maps, also known as state transition matrices (STMs). While moving forward through the nominal orbit, the deviation caused by a sufficiently large set of random maneuvers is propagated forward using the STM up until the time of the last observation. Each random maneuver is associated with a probability indicating the likelihood of its occurrence based on the residual between the last observation made and the propagated deviation using that maneuver. The key idea is that the likelihood is expected to concentrate

around one particular point in time as more measurements of the spacecraft position are obtained. Finally, the magnitude and direction of the maneuver can be recovered by assessing the likelihood of the time step exhibiting the highest probability.

A generic Bayesian framework to track lost-in-space non-cooperative maneuvering spacecraft, given bounds on maneuver parameters, such as maneuver time and maneuver magnitude, is shown in [19]. The approach of that work leverages polynomial approximations to efficiently and effectively approximate the non-linear dynamics associated with cislunar motion. The result is a general characterization of the resulting non-Gaussian probability density functions that are used to develop a search and tracking technique. Despite the approximation techniques used, this approach can still be computationally expensive, requiring tens of thousands of samples to be utilized. Conversely, the approach presented here requires a smaller number of models to be maintained by leveraging computational efficiencies gained through the use of analytic STMs. Zhou et al. [20] employ a modified state transition tensor that allows the orbit to be directly propagated under the effects of impulsive maneuver uncertainties, which can be used to estimate unknown impulsive maneuvers should the analytic STMs break down.

This technique follows an adaptive estimation setup based on MMAE. MMAE uses a parallel bank of filters to provide multiple estimates, where each filter corresponds with a dependence on some unknowns, which can be the process or measurement noise covariance elements if desired [3]. The state estimate is provided through a sum of each filter's estimate weighted by the likelihood of the unknown elements conditioned on the measurement sequence. The likelihood function gives the associated hypothesis that each filter is the correct one. MMAE approaches can easily become very computationally demanding if the filter bank is large. Although this burden can be reduced by parallelizing the filters, the approach presented here is enhanced by the computational efficiency of the STMs. Despite this replacement, the procedure can still be highly parallelized, thereby increasing the computational efficiency further.

The organization of this paper is as follows. First, a brief review of the problem is shown. Next, the main strategy used to solve the problem is developed. This includes how the MMAE is used along with the STMs for relative state propagation. Then, the approach for MD is derived based on the MMAE outputs. This includes both time as well as direction and magnitude estimation. The overall recursive-likelihood estimation for MD is then summarized in algorithm form. Finally, simulation results for both near-Earth and cislunar scenarios are shown.

II. Problem Setup

To formulate this problem more rigorously, consider a spacecraft on its nominal, or unperturbed, trajectory with mean inertial states $x_n(t) = [r_n^T \ \dot{r}_n^T]^T \in \mathbb{R}^6$, where $r_n, \dot{r}_n \in \mathbb{R}^3$ are implicit vector functions of time describing the mean position and velocity vectors, respectively, at an arbitrary time $t \in \mathbb{R}$. For an initial condition $x_0 \equiv x(t_0) = [r_0^T \ \dot{r}_0^T]^T$, they satisfy a second-order differential equation:

$$\ddot{r} = g(r) \tag{1}$$

Consider as well that observations, denoted as $y(t_k)$, are provided by sensors at discrete time intervals. In order to characterize the uncertainty of the states and measurements, statistical models for variation are assumed as follows:

$$dX_t = f(X_t)dt + \Sigma dW_t, \quad X(t_0) = X_0 \tag{2a}$$

$$Y_k = h(X_k) + Q_k \tag{2b}$$

Herein, the free motion of the spacecraft, represented by the random process X_t with random states $X(t)$, is described by a stochastic differential equation with drift model f, diffusion process W_t with constant spectral-density matrix $G = \Sigma\Sigma^T \in \mathbb{R}^{6\times6}$, and normally

distributed initial state $X_0 \sim N\{x_0, C_0\}$ with mean x_0 and error covariance $C_0 \equiv C(t_0) \in \mathbb{R}^{6\times6}$. The observation model h has additive measurement noise $Q_k \sim NID\{0, R\}$ with constant covariance $R \in \mathbb{R}^{3\times3}$ and discrete-time output measurements $Y_k \equiv Y(k\Delta t)$, where $k \in \mathbb{N}$ is a discrete time index and Δt is a time gap between observations.

The drift f in Eq. (2) is derived from the differential equation in Eq. (1), with the definition of g depending on the system under consideration. For instance, for analyzing maneuvers performed by Earth-orbiting spacecraft, g represents the acceleration experienced by the spacecraft, which, at minimum, is comprised of a central two-body attraction. Depending upon the time spanned between measurements, it may be needed to introduce corrections for the gravity field, such as the J_2 harmonic, aerodynamic drag, or solar radiation pressure. More complex scenarios include the effects of other celestial bodies, for which g might be derived from different versions of the three-body problem. As discussed in the Introduction, this work addresses the cases of MD in near-Earth Keplerian motion and in cislunar space. The main difference between the Keplerian case and any other case is that, in general, there will be no analytical solutions available for which a more general procedure is in place.

It is also sufficient to assume that only partial state information is available, meaning that only the position of the space object is directly measured. Therefore, the measurement equation h is defined here as follows:

$$h(x) \equiv [I_3 \ 0_3]x \tag{3}$$

where I_3 and 0_3 are 3×3 identity and zero matrices, respectively. Equipped with Eq. (2), consider now the last few consecutive times when observations have been taken after the spacecraft maneuvered, and let those times be gathered in an ordered set $\{t_o \in \mathbb{R}: o \in \{1, 2, \ldots, k\}\}$, such that $t_o < t_{o+1}$. The occurrence of a spacecraft maneuver at an unknown time $t_m \in [t_0, t_1]$ can cause significant statistical errors between the estimated outputs $\hat{y}(t_1), \hat{y}(t_2), \ldots, \hat{y}(t_k)$ and the actual measurements $y(t_1), y(t_2), \ldots, y(t_k)$. These errors are accentuated the larger the time difference $(t_o - t_m)$, meaning the longer it takes to observe the spacecraft after it has maneuvered. In such cases, one can reasonably expect DA to become more challenging or even to lose track of the spacecraft as a consequence.

The propagation of the nominal (unperturbed) states of the system can be performed by adopting different strategies. The most common is by discretizing the stochastic differential equation and propagating using an EKF formulation. To that end, the steps within the EKF are shown in Table 1 for future reference. In the next sections, a methodology is presented to determine the execution time t_m of the impulsive maneuver, along with the magnitude and direction of the maneuver vector ΔV in an efficient manner.

Table 1 State propagation using the extended Kalman filter

Initialize
$\hat{x}(t_0) = E[X_0] = x_0$
$C(t_0) = E[(X_0 - x_0)(X_0 - x_0)^T] = C_0$
Gain
$H_k = \nabla h(\hat{x}_k^-) = [I_3 \ 0_3]$
$K_k = C_k^- H_k^T [H_k C_k^- H_k^T + R]^{-1}$
Update
$\hat{x}_k^+ = \hat{x}_k^- + K_k[y_k - H_k \hat{x}_k^-]$
$C_k^+ = [I_6 - K_k H_k]C_k^-$
Propagate
$\dfrac{d}{dt}\hat{x}(t) = f(\hat{x}(t))$
$A(t) \equiv \nabla f(\hat{x}(t))$
$\dfrac{d}{dt}C(t) = A(t)C + CA(t)^T + G$

III. Maneuver Determination Approach

The process of fully determining an impulsive maneuver is threefold: at each point of the spacecraft's nominal path, the position is projected forward in time by hypothesized multiple maneuvers, the likelihood of each prediction is computed afterward based on observational data, and it is used to estimate the maneuver and time of execution. Central to this approach is a multiple-model adaptive estimation (MMAE) process. MMAE is a recursive estimation technique commonly applied as a parallel bank of M filters, with each filter operating under a different hypothesis for some system unknown [7]. In this work, two unknown quantities are addressed: an instantaneous change in velocity vector that can cause deviations from the spacecraft's nominal trajectory and the time at which the velocity change has been executed. This is then combined with relative linear models to improve the performance of the time propagation. These future predictions enable the calculation of the most likely value for the unknown quantities, based on the current and past observations.

The detailed explanation of the approach is as follows. First, a searching space for the unknown quantities is defined. The actual impulsive maneuver can be assumed to be a three-dimensional vector $\Delta V \in \mathbb{R}^3$, representing the instantaneous change in velocity with the estimator denoted as $\hat{\theta} \in \mathbb{R}^3$. Let $\tilde{\Theta}$ characterize a set of possible maneuvers such that $\Delta V \in \tilde{\Theta}$. That is,

$$\tilde{\Theta} \equiv \{\theta \in \mathbb{R}^3 : \theta_{\min} \le \|\theta\| \le \theta_{\max}\}, \quad 0 < \theta_{\min} \le \theta_{\max} \quad (4)$$

where $\theta_{\min}$ and $\theta_{\max}$ are assumed values for the minimum and maximum magnitudes of the actual maneuver, respectively. The set $\tilde{\Theta}$ is the searching space for $\hat{\theta}$, and can be more or less conservative depending on the chosen values for $\theta_{\min}$ and $\theta_{\max}$. Note that the time of execution of the maneuver is also unknown but constrained since $t_m \in [t_0, t_1]$, given that the first observation y_1 at time t_1 already suggests the occurrence of a maneuver. The interval $[t_0, t_1]$ is, therefore, the searching space for the estimator of t_m, which will be denoted as $\hat{\tau}$. Subsequently, some observations of the spacecraft after maneuvering are required. The recursive algorithm for MD will iterate once for every observation gathered and can continue to iterate for every new observation obtained thereafter. The more observations, the better the accuracy of the estimation.

It is important to note that this approach assumes perfect association of the measurements to the object orbit of interest. Traditionally, this association, referred to as measurement-to-track association [21], utilizes statistical comparisons between the propagated orbit, projected into the observation space and the measurements. However, for the problem of maneuver detection, the propagated orbit will necessarily prohibit association. Fortunately, other methods of association exist. For example, tracklet-to-orbit association has been shown in [22], using optimal control theory coupled with an admissible region that does not require perfect knowledge of the current orbit. Other methods leverage data independent of the orbital state. Unresolved photometry [23] and hyperspectral imaging [24] have also proven useful to aid in measurement-to-track association through the generation of historical patterns-of-life or "fingerprints" of known satellites. Statistical reasoning and/or machine learning techniques can then be leveraged to determine if the photometric signature of an observed object associates with a known object [25].

Based on the previous discussion, reachability formulations would provide rigorous frameworks for the mathematical analysis of the time evolution of sets in this work. Set propagation is relevant, since it would allow us to take any point of the nominal trajectory of the spacecraft, e.g., $x_n(\tau)$, and perturb it with all the admissible maneuvers to define a set $\mathcal{X}_\tau$ for every $\tau \in [t_0, t_1]$. If the admissible maneuvers represent here vectors of (instantaneous) change in velocity, $\theta \in \tilde{\Theta}$, then the set $\mathcal{X}_\tau$ is defined for every time $\tau \in [t_0, t_1]$ as

$$\mathcal{X}_\tau \equiv \{x = [r^T \ \dot{r}^T]^T \in \mathbb{R}^6 : r = r_n(\tau), \dot{r} = \dot{r}_n(\tau) + \theta, \ \forall \ \theta \in \tilde{\Theta}\} \quad (5)$$
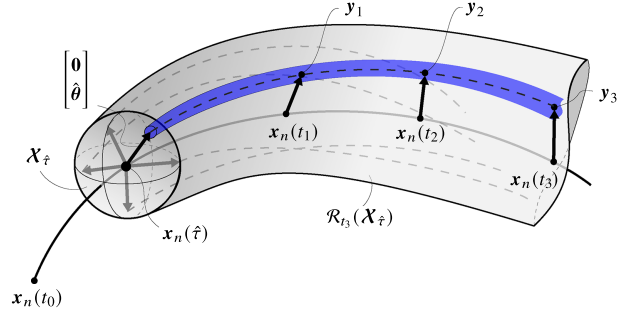

Fig. 1 Representation of the reachability of the set $\mathcal{X}_{\hat{\tau}}$.

The forward propagation in time of the set $\mathcal{X}_\tau$, denoted as $\mathcal{R}_{t_k}(\mathcal{X}_\tau)$ and depicted in Fig. 1 as the gray tube, defines the reachability of the set $\mathcal{X}_\tau$ until the time t_k, i.e., all the states that the spacecraft can reach up to the time of the last measurement t_k if the spacecraft maneuvers at time τ. The reachable set of $\mathcal{X}_\tau$ directly tells possible times at which a maneuver took place by examining a sequence of observations of the spacecraft after maneuvering, represented in Fig. 1 by the points y_1, y_2, and y_3. If for a given time τ the reachable set $\mathcal{R}_{t_3}(\mathcal{X}_\tau)$ up to time t_3 contains all three measurements, then it means that at time τ there are maneuvers in $\tilde{\Theta}$ that can make the spacecraft reach the observation points, and thus τ is a candidate maneuvering time.

Notice, however, that one maneuver could make the spacecraft reach some of the measurement points, but not the entire sequence. The true maneuver, hence, is estimated by that one vector $\hat{\theta} \in \tilde{\Theta}$ that, applied at a specific time $\hat{\tau} \in [t_0, t_1]$, makes the perturbed trajectory of the spacecraft visit all the measurement points. Unfortunately, computing the reachable set $\mathcal{R}_t(\mathcal{X}_\tau)$ requires complex analytical formulations and approximations (both in the deterministic and the stochastic setup) that are cumbersome and very computationally demanding and thus are left out of the scope of this paper. It is possible, however, to design a feasible and more practical approach by discretizing the problem, namely, by defining a finite version of the searching sets $\tilde{\Theta}$ and $[t_0, t_1]$. Consequently, a large positive but finite parameter $M \in \mathbb{R}$ and a step-size $\Delta t_s \in \mathbb{R}$ yield the following set of discrete times:

$$T_{\Delta t_s} \equiv \{t_0, t_0 + \Delta t_s, t_0 + 2\Delta t_s, \ldots, t_0 + K\Delta t_s\},$$
$$K = \text{ceil}\left[\frac{(t_1 - t_0)}{\Delta t_s}\right], \quad \Delta t_s > 0 \quad (6)$$

where ceil[·] is the ceiling operator that rounds the argument to the next integer greater than the argument. The finite family of maneuvers Θ_M that approximate the continuous set $\tilde{\Theta}$ by uniformly[§] picking elements from Eq. (4):

$$\Theta_M \equiv \{\theta_1, \ldots, \theta_M\}, \text{ such that } \theta_j \in \tilde{\Theta},$$
$$\forall j \in \{1, \ldots, M\} \text{ and } 0 < M < +\infty \quad (7)$$

As previously mentioned, the recursive algorithm for MD will iterate once for every observation; this constitutes an outer loop on the observations. An inner loop is defined to iterate along the times in $T_{\Delta t_s}$. At each time $\tau_i \in T_{\Delta t_s}$, the nominal state of the spacecraft, $x_n(\tau_i)$, is perturbed by each velocity vector in the finite set Θ_M to generate M points, or particles. Let these particles be denoted as $x_{i,j}(\tau_i)$, given the jth change in velocity vector performed at the ith time of execution:

$$x_{i,j}(\tau_i) = \begin{bmatrix} r_n(\tau_i) \\ \dot{r}_n(\tau_i) + \theta_j \end{bmatrix}, \quad \forall \ \theta_j \in \Theta_M \quad (8)$$

[§]Note that sampling uniformly from a sphere is not straightforward, and specific methods exist in the literature [26].

The particle is then propagated forward in time, along with its error covariance, until the time of each observation, e.g., $t_1, t_2, \ldots, t_k$, carrying the information that at time τ_i a hypothetical change in velocity $\boldsymbol{\theta}_j$ occurred. Propagation is performed by means of STMs, which enables a straightforward relation between the state vector of a particle at two different times. Instead of propagating the entire state vector $\boldsymbol{x}_{i,j}(\tau_i)$, the STMs propagate the deviations with respect to the nominal trajectory.

Take, for instance, the example showcased in Fig. 2 and assume that only the observation $\boldsymbol{y}_1$ is available. The algorithm will iterate once through every element in $\boldsymbol{T}_{\Delta t_s}$, generating M particles at each time. For every $\tau_i \in \boldsymbol{T}_{\Delta t_s}$, the STM is used to determine the positional deviation at time t_1 of every particle and the error covariance associated to those predictions. The positional deviation caused by a particular change in velocity $\boldsymbol{\theta}_j \in \boldsymbol{\Theta}_M$ applied at an arbitrary time τ_i is represented in Fig. 2 as the gray vector $\boldsymbol{\rho}_{i,j}^-(t_1)$, alongside its respective error covariances $C_{i,j}^-(t_1)$ represented as an ellipsoid. The positional deviation at time t_1 caused by the remaining velocity vectors, i.e., $\boldsymbol{\Theta}_M \backslash \{\boldsymbol{\theta}_j\} \equiv \{\boldsymbol{\theta}_1, \ldots, \boldsymbol{\theta}_{i-1}, \boldsymbol{\theta}_{i+1}, \ldots, \boldsymbol{\theta}_M\}$, applied also at time τ_i, is depicted as a cloud of gray dots in the near region. Note that each of these dots has an associated error covariance, although they are not shown for clarity. Notice as well that the cloud of propagated particles at t_1 will be different for every time τ_i considered. For some τ_i and $\boldsymbol{\theta}_j$, the position of the propagated particle will fall very far from the observation $\boldsymbol{y}_1$ of the spacecraft position. The conditional probability $P(\tau_i, \boldsymbol{\theta}_j | \boldsymbol{y}_1)$ is used to assess the correlation between the pair $(\tau_i, \boldsymbol{\theta}_j)$ and the observation $\boldsymbol{y}_1$, indicating the probability that the time of the actual maneuver t_m and the change in velocity $\Delta \boldsymbol{V}$ are characterized by those same τ_i and $\boldsymbol{\theta}_j$. When a new observation $\boldsymbol{y}_2$ comes along, the algorithm will iterate once again in the same manner and will use the conditional probability $P(\tau_i, \boldsymbol{\theta}_j | \boldsymbol{y}_1)$ previously computed to calculate the conditional probability $P(\tau_i, \boldsymbol{\theta}_j | \boldsymbol{y}_1, \boldsymbol{y}_2)$, updating the knowledge of the pairs $(\tau_i, \boldsymbol{\theta}_j)$.

Assuming that no statistical information of the actual maneuver time, magnitude, and direction is available, all elements in $\boldsymbol{\Theta}_M$ are initially considered to have equal probability of characterizing the vector $\Delta \boldsymbol{V}$, as well as all times in $\boldsymbol{T}_{\Delta t_s}$ are equally likely to be the true maneuver time t_m. Therefore, the prior joint probability $P(\tau_i, \boldsymbol{\theta}_j)$ can be assumed to be

$$P(\tau_i, \boldsymbol{\theta}_j) = P(\tau_i)P(\boldsymbol{\theta}_j) = \frac{1}{K+1}\frac{1}{M} \tag{9}$$

which satisfies

$$\sum_{i=1}^{K+1}\sum_{j=1}^{M} P(\tau_i, \boldsymbol{\theta}_j) = 1 \tag{10}$$

It is clear that information is lost due to the discretization of the problem, and the resolution of the results will directly depend on the selected values for K (actually, Δt_s) and M, posing a tradeoff between efficiency and accuracy.
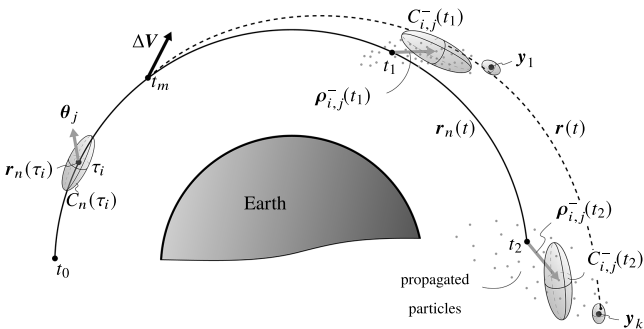

Fig. 2   Diagram of an instance in the MD algorithm.

A.   Recursive Likelihood Estimation

The conditional probability $P(\tau_i, \boldsymbol{\theta}_j | \boldsymbol{\mathcal{Y}}_k)$, where $\boldsymbol{\mathcal{Y}}_k \equiv \{\boldsymbol{y}_1, \boldsymbol{y}_2, \ldots \boldsymbol{y}_k\}$ is the set of all measurements received up to time t_k, is used to assess the correctness of the hypothesized maneuver and time of execution. Using Bayes rule, this conditional probability can be expressed as

$$\begin{aligned}
P(\tau_i, \boldsymbol{\theta}_j | \boldsymbol{\mathcal{Y}}_k) &= \frac{P(\boldsymbol{\mathcal{Y}}_k | \tau_i, \boldsymbol{\theta}_j)P(\tau_i, \boldsymbol{\theta}_j)}{P(\boldsymbol{\mathcal{Y}}_k)} \\
&= \frac{P(\boldsymbol{\mathcal{Y}}_k | \tau_i, \boldsymbol{\theta}_j)P(\tau_i, \boldsymbol{\theta}_j)}{\sum_{i=1}^{K+1}\sum_{j=1}^{M} P(\boldsymbol{\mathcal{Y}}_k | \tau_i, \boldsymbol{\theta}_j)P(\tau_i, \boldsymbol{\theta}_j)},
\end{aligned}$$
$$\forall i \in \{0, \ldots, K\}, \quad \forall j \in \{1, \ldots, M\} \tag{11}$$

Under the assumption that the observations are independent, the numerator of Eq. (11) can be cast as a recursion:

$$\begin{aligned}
P(\boldsymbol{\mathcal{Y}}_k | \tau_i, \boldsymbol{\theta}_j) &= P(\boldsymbol{y}_k, \boldsymbol{\mathcal{Y}}_{k-1} | \tau_i, \boldsymbol{\theta}_j) \\
&= P(\boldsymbol{y}_k | \tau_i, \boldsymbol{\theta}_j)P(\boldsymbol{\mathcal{Y}}_{k-1} | \tau_i, \boldsymbol{\theta}_j) \tag{12}
\end{aligned}$$

Equation (11) then becomes

$$P(\tau_i, \boldsymbol{\theta}_j | \boldsymbol{\mathcal{Y}}_k) = \frac{P(\boldsymbol{y}_k | \tau_i, \boldsymbol{\theta}_j)P(\boldsymbol{\mathcal{Y}}_{k-1} | \tau_i, \boldsymbol{\theta}_j)P(\tau_i, \boldsymbol{\theta}_j)}{\sum_{i=1}^{K+1}\sum_{j=1}^{M} P(\boldsymbol{y}_k | \tau_i, \boldsymbol{\theta}_j)P(\boldsymbol{\mathcal{Y}}_{k-1} | \tau_i, \boldsymbol{\theta}_j)P(\tau_i, \boldsymbol{\theta}_j)} \tag{13}$$

Notice that the forward propagation of the particles in Eq. (8) depends directly on the maneuver $\boldsymbol{\theta}_j$ and time τ_i. However, it also depends indirectly on the subset $\boldsymbol{\mathcal{Y}}_0$, i.e., all the measurements taken prior to the spacecraft maneuvering, because the nominal trajectory is estimated using previous collected observations since t_0 by the EKF algorithm. As such, the conditional probability $P(\boldsymbol{y}_k | \tau_i, \boldsymbol{\theta}_j)$ can be expressed as $P(\boldsymbol{y}_k | \boldsymbol{x}_{i,j}^-(t_k))$, where $\boldsymbol{x}_{i,j}^-(t_k)$ is the *a priori* state estimate of a filter (based on the previous observations, i.e., $\boldsymbol{\mathcal{Y}}_0$) operating on the hypothesis $(\tau_i, \boldsymbol{\theta}_j)$. In this form it is easy to see that this probability is the likelihood of $\boldsymbol{y}_k$, which can be readily computed:

$$\begin{aligned}
P(\boldsymbol{y}_k | \boldsymbol{x}_{i,j}^-(t_k)) &= \frac{1}{\sqrt{\det(2\pi\mathcal{E}_{i,j}^-(t_k))}} \\
&\times \exp\left(-\frac{1}{2}\boldsymbol{e}_{i,j}^-(t_k)^T \mathcal{E}_{i,j}^-(t_k)^{-1} \boldsymbol{e}_{i,j}^-(t_k)\right) \tag{14}
\end{aligned}$$

where $\boldsymbol{e}_{i,j}^-(t_k)$ is the measurement-minus-estimate residual from the EKF:

$$\boldsymbol{e}_{i,j}^-(t_k) = \boldsymbol{y}(t_k) - \boldsymbol{y}_{i,j}^-(t_k) = \boldsymbol{y}_k - \boldsymbol{h}(\boldsymbol{x}_{i,j}^-(t_k)) \tag{15}$$

and $\mathcal{E}_{i,j}^-(t_k)$ is the associated innovations covariance:

$$\mathcal{E}_{i,j}^-(t_k) = E\left[\boldsymbol{e}_{i,j}^-(t_k)\boldsymbol{e}_{i,j}^-(t_k)^T\right] = HC_{i,j}^-(t_k)H^T + R \tag{16}$$

Note that $E[\cdot]$ denotes expectation. Given the observation function in Eq. (3), the Jacobian is given by $H \equiv \nabla\boldsymbol{h} = [I_3 \quad 0_3]$.

The estimated particle states $\boldsymbol{x}_{i,j}^-(t_k)$ and error covariances $C_{i,j}^-(t_k)$ are usually computed by means of a bank of EKFs in the MMAE process. Recall from Table 1 that the time propagation of both state and error covariance is conducted by numerical approximations of the integrals

$$\boldsymbol{x}_{i,j}^-(t_k) = \boldsymbol{x}_{i,j}^-(\tau_i) + \int_{\tau_i}^{t_k} \boldsymbol{f}(\boldsymbol{x}(t))\,\mathrm{d}t \tag{17a}$$

$$C_{i,j}^-(t_k) = C_{i,j}^-(\tau_i) + \int_{\tau_i}^{t_k} (A(t)C(t) + C(t)A(t)^T + G)\,\mathrm{d}t \tag{17b}$$

Instead, state-transition matrices or STMs, $\Phi(t_1, t_0)$, are leveraged to propagate the initial state vector and error covariance, i.e., $x_{i,j}^-(\tau_i)$ and $C_{i,j}^-(\tau_i)$, directly to the times at which new measurements are taken:

$$x_{i,j}^-(t_k) = x_n^-(t_k) + \Phi(t_k, \tau_i)\left[x_{i,j}^-(\tau_i) - x_n^-(\tau_i)\right] \tag{18a}$$

$$C_n^-(t_k) = \Phi(t_k, \tau_i)C_n^-(\tau_i)\Phi(t_k, \tau_i)^T + \Delta t G \tag{18b}$$

where $x_n^-(\cdot)$ and $C_n^-(\cdot)$ are the nominal or unperturbed state and error covariance estimation from the EKF.

A straightforward advantage of this approach is that analytical versions of STMs that encode the central two-body attraction are readily available in the literature. To incorporate further sources of disturbance, such as J_2, aerodynamic drag, solar radiation pressure, or other celestial bodies, a more generalized procedure is required, which involves the numerical integration of the STM [27]. However, only one integration per element in $T_{\Delta t_s}$ is needed in order to propagate all the particles to the time of the first measurement (i.e., a total of $K + 1$), whereas the standard way would require integrating the equations of each particle (i.e., a total of $(K + 1)M$). Note that in the latter, the integration procedure becomes increasingly expensive with the amount of particles considered. Additionally, only one extra integration is required for any subsequent measurement collected, due to the concatenating properties of the STMs. In light of new observations at times $t_2, t_3, \ldots, t_k$, only one STM needs to be integrated per observation, provided that

$$\Phi(t_2, \tau_i) = \Phi(t_2, t_1)\Phi(t_1, \tau_i),$$
$$\Phi(t_3, \tau_i) = \Phi(t_3, t_2)\Phi(t_2, t_1)\Phi(t_1, \tau_i),$$
$$\Phi(t_k, \tau_i) = \Phi(t_k, t_{k-1}) \cdots \Phi(t_3, t_2)\Phi(t_2, t_1)\Phi(t_1, \tau_i) \tag{19}$$

B. Relative State Propagation

State propagations are a linearization of the equations of motion around a reference or nominal path; in this case, the unperturbed trajectory between t_0 and t_k is regarded here as referential or nominal. STMs do not yield exact solutions but provide fast, direct, and easy-to-compute approximations that can retain accuracy under some conditions. Consider an autonomous system governed by an ordinary differential equation of the following form:

$$\frac{d}{dt}x = A(t)x \tag{20}$$

for a general n-vector x. A solution for the time evolution of $x(t)$ is given by

$$x(t) = \Phi(t, t_0)x(t_0) \tag{21}$$

where $\Phi(t, t_0)$ is the STM of the system. The STM at any time t is given by the solution to the matrix differential equation [28]:

$$\frac{d}{dt}\Phi(t, t_0) = A(t)\Phi(t, t_0), \quad \Phi(t_0, t_0) = I_6 \tag{22}$$

For the MD problem, the evolution of the difference between the hypothesized maneuver and the nominal path, $\rho(t) = r(t) - r_n(t)$, is needed. Given that spacecraft motion is governed by a second-order differential equation (recall that $\ddot{r} = g(r)$) the full relative state is given by

$$\delta x(t) \equiv \begin{bmatrix} \rho(t) \\ \dot{\rho}(t) \end{bmatrix} = \begin{bmatrix} r(t) - r_n(t) \\ \dot{r}(t) - \dot{r}_n(t) \end{bmatrix} \tag{23}$$

The state-space matrix $A(t)$ generally has the subsequent structure of an integrator, given by

$$A(t) = \begin{bmatrix} 0_3 & I_3 \\ \Xi(t) & 0_3 \end{bmatrix} \tag{24}$$

where the expression of $\Xi(t)$ depends on the environmental forces accounted in g and the nominal trajectory of the spacecraft. The expression for the STM at an arbitrary time t is obtained by numerical integration of Eq. (22), together with differential equation in Eq. (1) due to the dependency of $A(t)$ in the nominal path.

Finally, it is possible to express the state deviation at time t_k, given the initial deviation in velocity θ_j at a time τ_i, by means of the STM. Consulting Eq. (23) at time τ_i, the instant the maneuver is applied, the relative state is

$$\delta x_{i,j}^-(\tau_i) = \begin{bmatrix} 0 \\ \theta_j \end{bmatrix} \tag{25}$$

Therefore

$$\delta x_{i,j}^-(t_k) \equiv \begin{bmatrix} \rho_{i,j}^-(t_k) \\ \dot{\rho}_{i,j}^-(t_k) \end{bmatrix} = \Phi(t_k, \tau_i)\begin{bmatrix} 0 \\ \theta_j \end{bmatrix},$$
$$\forall i \in \{0, 1, \ldots, K\} \text{ and } \forall j \in \{1, \ldots, M\} \tag{26}$$

The state prediction at t_k can then be approximated as

$$x_{i,j}^-(t_k) = x_n(t_k) + \delta x_{i,j}^-(t_k) \tag{27}$$

The procedure to determine the error covariance $C_{i,j}^-(t_k)$ associated to $x_{i,j}^-(t_k)$ will be covered in the next sections.

It is important to remark that integration is not always required to determine the STM. Multiple versions of closed-form solutions exist in the literature for the central-body problem [28–31], defined in multiple reference frames and with different degrees of accuracy. For some analyses, however, STMs are found through integration of Eq. (22). Some examples include long observation gaps and maneuvers performed in cislunar space. The procedure to determine the STM thus depends on the particular problem. Two different scenarios are studied here: one where integration is necessary and another one where it is not. The procedures to determine the STM are described in each case, respectively; other scenarios not explored here can be inferred from one of these two. Some of the relevant properties of STMs that will become instrumental are given by

$$\Phi(t, t) = I_6 \tag{28a}$$

$$\Phi(t_1, t_0) = \Phi^{-1}(t_0, t_1) \tag{28b}$$

$$\Phi(t_2, t_0) = \Phi(t_2, t_1)\Phi(t_1, t_0) \tag{28c}$$

1. Near-Earth Space

The most fundamental scenario is that of a spacecraft orbiting near Earth driven solely by the effects of gravity. To that end, the two-body problem is defined by a single symmetrical force vector g_E, and the spacecraft is governed by the following second-order differential equation:

$$\ddot{r} = g_E(r) = -\mu_\oplus \frac{r}{\|r\|^3} \tag{29}$$

where $\mu_\oplus \in \mathbb{R}$ is Earth's gravitational constant, and $r \in \mathbb{R}^3$ is the absolute spacecraft position vector. If the maneuvered motion remains close to the unperturbed (nominal) trajectory (i.e., a relative distance significantly smaller than the orbital radius) then a first-order approximation of the relative motion can be used. This linear description of the relative motion is known as the Clohessy–Wiltshire (C-W) equations. The Jacobian $A(t)$ of Eq. (24) evaluated at the nominal trajectory has linearized dynamics given by

$$\Xi(t) = \frac{\partial \boldsymbol{g}_E(\boldsymbol{r})}{\partial \boldsymbol{r}}\bigg|_{\boldsymbol{r}=\boldsymbol{r}_n} = \frac{\mu_\oplus}{\|\boldsymbol{r}_n\|^3}\left(\frac{3\boldsymbol{r}_n\boldsymbol{r}_n^T}{\|\boldsymbol{r}_n\|^2} - I_3\right) \quad (30)$$

The particularity of this model is that it permits an analytic solution for the STM, thereby mitigating the need to numerically integrate Eq. (22). One such analytic solution is presented in [31], which shows the STM as a matrix product, expressed in the Earth-centered inertial (ECI) frame:

$$\Phi(t_k, \tau_i) = \Gamma(\boldsymbol{r}_n(t_k), \dot{\boldsymbol{r}}_n(t_k), \Delta t_i)\Gamma^{-1}(\boldsymbol{r}_n(\tau_i), \dot{\boldsymbol{r}}_n(\tau_i), 0) \quad (31a)$$

$$\Gamma(\boldsymbol{r}, \dot{\boldsymbol{r}}, \Delta t_i) = \begin{bmatrix} [\boldsymbol{r}\times] & -([\boldsymbol{r}\times][\dot{\boldsymbol{r}}\times] + [\boldsymbol{\ell}\times])B & -\boldsymbol{r} + \frac{3}{2}\dot{\boldsymbol{r}}\Delta t_i \\ [\dot{\boldsymbol{r}}\times] & \left(\frac{\mu}{r^3}[\boldsymbol{r}\times]^2 - [\dot{\boldsymbol{r}}\times]\right)B & -\frac{3}{2}\frac{\mu}{r^3}\boldsymbol{r}\Delta t_i + \frac{1}{2}\dot{\boldsymbol{r}} \end{bmatrix}$$
$$(31b)$$

where $[\cdot\times]$ is a skew-symmetric matrix defined as

$$[\boldsymbol{\omega}\times] \equiv \begin{bmatrix} 0 & -\omega_z & \omega_y \\ \omega_z & 0 & -\omega_x \\ -\omega_y & \omega_x & 0 \end{bmatrix} \quad (32)$$

for any three-dimensional vector $\boldsymbol{\omega} = [\omega_x, \omega_y, \omega_z]^T$, $\boldsymbol{\ell} = \boldsymbol{r}_n \times \dot{\boldsymbol{r}}_n$ is the angular momentum vector of the unperturbed (nominal) orbit, and $B \in \mathbb{R}^{3\times 2}$ is a full-rank matrix that satisfies $\boldsymbol{\ell}^T B = 0$. The time increment from the initial relative state $\boldsymbol{\rho}(\tau_i)$ to the mapped state $\boldsymbol{\rho}(t_k)$ is $\Delta t_i = t_k - \tau_i$. Equation (31) shows that Φ depends on the unperturbed, reference or nominal, trajectories $\boldsymbol{r}_n$ and $\dot{\boldsymbol{r}}_n$, determined by integrating Eq. (29). Note that those are the solutions of the two-body problem, which also has a known closed form. Therefore, numerical integration of the nominal spacecraft states can be avoided as well, for any time in the interval $[t_0, t_k]$.

The propagated error covariance matrix of the perturbed states $C^-_{i,j}(t_k)$ can also be determined using the STM. To that end, the nominal error covariance at the maneuvering time $C_n(\tau_i)$, which is assumed to be known from the standard EKF, is propagated forward using a second STM, given by

$$\Phi'(t_k, \tau_i; \boldsymbol{\theta}_j) = \Gamma\big(\boldsymbol{r}_n(t_k) + \boldsymbol{\rho}^-_{i,j}(t_k), \dot{\boldsymbol{r}}_n(t_k) + \dot{\boldsymbol{\rho}}^-_{i,j}(t_k), \Delta t_i\big)$$
$$\times \Gamma^{-1}\big(\boldsymbol{r}_n(\tau_i), \dot{\boldsymbol{r}}_n(\tau_i) + \boldsymbol{\theta}_j, 0\big) \quad (33)$$

The previous expression for Φ' takes the hypothesized trajectory perturbed by the pair $(\tau_i, \boldsymbol{\theta}_j)$ as the *nominal* trajectory in order to propagate the error covariance of the particle as

$$C^-_{i,j}(t_k) = \Phi'(t_k, \tau_i; \boldsymbol{\theta}_i)C_n(\tau)\Phi'(t_k, \tau_i; \boldsymbol{\theta}_i)^T + \Delta t_i G \quad (34)$$

Equations (29–34) represent a tradeoff between computational efficiency and accuracy, provided that this model disregards many perturbing effects (aerodynamic drag, gravity gradient, other celestial bodies, etc.).

2. Cislunar Space

As a spacecraft's distance from Earth increases, the gravitational pull of the moon becomes non-negligible. In this region, generally accepted to be spacecraft above three to four geostationary radii, the equations of motion are a complex combination that simultaneously considers the motion of the spacecraft as well as the Earth and moon. The equations governing the motion of a spacecraft in cislunar space are known as the three-body equations and exhibit very rare cases where analytical solutions can be determined. In general, solving them requires numerical integration, which worsens the computational efficiency of the MD algorithm presented here compared to near-Earth cases.

Consider the Earth and moon as the only celestial bodies interacting with the spacecraft. The following second-order differential equation describes the acceleration of the spacecraft, expressed in an inertial frame:

$$\ddot{\boldsymbol{r}} = \boldsymbol{g}_{EM}(\boldsymbol{r}) = -\mu_\oplus \frac{\boldsymbol{r} - \boldsymbol{r}_1}{\|\boldsymbol{r} - \boldsymbol{r}_1\|^3} - \mu_\ominus \frac{\boldsymbol{r} - \boldsymbol{r}_2}{\|\boldsymbol{r} - \boldsymbol{r}_2\|^3} \quad (35)$$

Herein, $\mu_\ominus \in \mathbb{R}$ is the gravitational constant of the moon. The positional vectors $\boldsymbol{r}_1$ and $\boldsymbol{r}_2$ represent Earth and moon absolute positions, respectively. It is often convenient to describe the previous dynamics in a rotating, or synodic, reference frame and assume that the Earth and the moon trace out circular orbits about their common center of mass, or barycenter. Under this condition, $\boldsymbol{r}_1$ and $\boldsymbol{r}_2$ are fixed, and Coriolis and centrifugal accelerations enter the equations of motion. The resulting equations of motion are known as the circular restricted three-body problem (CR3BP):

$$\ddot{\boldsymbol{r}}' = \boldsymbol{g}_{EM}(\boldsymbol{r}') - 2(\boldsymbol{\Omega} \times \dot{\boldsymbol{r}}') - \boldsymbol{\Omega} \times (\boldsymbol{\Omega} \times \boldsymbol{r}') \quad (36)$$

where now $\boldsymbol{r}'$ and $\dot{\boldsymbol{r}}'$ are the spacecraft's position and velocity vectors expressed in the synodic reference frame. The vector $\boldsymbol{\Omega} \in \mathbb{R}^3$ is the angular velocity of the Earth–moon system, which is constant due to the assumption of circular motion.

The non-Keplerian space is characterized by having highly nonlinear regimes. However, under some similar conditions to the C-W equations, one can simplify the relative equations of motion emerging from the time derivative of Eq. (23). If the distance between the maneuvered and nominal trajectories of the spacecraft is significantly smaller than the distance between the maneuvered trajectory and the celestial bodies, then a first-order approximation of the relative dynamics can be leveraged. The Jacobian matrix $A'(t)$ of the system in Eq. (36) is then

$$A'(t) = \begin{bmatrix} 0_3 & I_3 \\ \Xi(t) & -2[\boldsymbol{\Omega}\times] \end{bmatrix} \quad (37)$$

Note that this state-space matrix $A'(t)$ and the one introduced in Eq. (24) have a similar structure and only differ in the Coriolis term, i.e., the bottom-right submatrix $-2[\boldsymbol{\Omega}\times]$, appearing now due to the fact that the spacecraft motion is being mathematically described in a rotating frame. The submatrix $\Xi(t)$ is given by

$$\Xi(t) = \frac{\mu_\oplus}{|\boldsymbol{\rho}_1|^3}\left(\frac{3\boldsymbol{\rho}_1\boldsymbol{\rho}_1^T}{|\boldsymbol{\rho}_1|^2} - I_3\right) + \frac{\mu_\ominus}{|\boldsymbol{\rho}_2|^3}\left(\frac{3\boldsymbol{\rho}_2\boldsymbol{\rho}_2^T}{|\boldsymbol{\rho}_2|^2} - I_3\right) - [\boldsymbol{\Omega}\times][\boldsymbol{\Omega}\times]$$
$$(38)$$

where the nominal position vector of the spacecraft with respect to the Earth is defined as $\boldsymbol{\rho}_1 \equiv \boldsymbol{r}'_n - \boldsymbol{r}'_1$, while $\boldsymbol{\rho}_2 \equiv \boldsymbol{r}'_n - \boldsymbol{r}'_2$ is with respect to the moon, both expressed in the synodic frame.

Finally, the STM is derived by numerical integration of the following differential equations from $t = \tau$ until $t = t_k$, for given initial conditions (recall that $\Phi(\tau, \tau) = I_6$):

$$\frac{d}{dt}\boldsymbol{r}'_n(t) = \dot{\boldsymbol{r}}'_n(t) \quad (39a)$$

$$\frac{d}{dt}\dot{\boldsymbol{r}}'_n(t) = \boldsymbol{g}_{EM}(\boldsymbol{r}'_n(t)) - 2\{\boldsymbol{\Omega} \times \dot{\boldsymbol{r}}'_n(t)\} - \boldsymbol{\Omega} \times \{\boldsymbol{\Omega} \times \boldsymbol{r}'_n(t)\} \quad (39b)$$

$$\frac{d}{dt}\Phi(t, \tau) = A'(t)\Phi(t, \tau) \quad (39c)$$

Computing the STM involves a numerical integration of Eq. (39), which can be computationally expensive. However, computations can be reduced by taking advantage of the concatenating property of the STM shown in Eq. (19). Because the STM can at any time be computed from previous values, already computed STMs are stored in memory while awaiting the arrival of new observations. Therefore, the receipt of each new observation requires only one STM to be computed via integration.

The error covariance matrix of the perturbed states $C_{i,j}^-(t_k)$ is more intricate to determine in the general case. There exist several ways to do so, yet it is convenient to involve the STM as much as possible to promote efficiency. Therefore, it is proposed to use the unscented transform (UT) [32] to project the error covariance forward in time. The proposed formulation is as follows. First, a set of sigma points is computed in a column matrix. For that, consider the column vector $\delta x_{i,j}(\tau_i) = [0^T \; \theta_i^T]^T$ describing a deviation from the nominal path at time τ_i by a change in velocity θ_j:

$$\chi(\tau_i) = \Big[\delta x_{i,j}(\tau_i), \delta x_{i,j}(\tau_i) + \gamma \sqrt{C_n(\tau_i) + G},$$
$$\delta x_{i,j}(\tau_i) - \gamma \sqrt{C_n(\tau_i) + G} \Big] \qquad (40)$$

where $C_n(\tau_i)$ is the nominal error covariance at time τ_i, and G is the process spectral-density matrix. The notation $\sqrt{A}$ for a matrix A, is understood in the sense of the Cholesky decomposition. Recall from the UT that the scalar $\gamma = \sqrt{n + \lambda}$, where $n = 6$ is the dimension of the state vector and λ is a tuning parameter. The notation $\chi_\ell(\tau)$ will refer to the sigma point in the ℓth column of Eq. (40), which is propagated again by means of the STM to obtain deviations at time t_k:

$$\chi_\ell(t_k) = \Phi(t_k, \tau)\chi_\ell(\tau), \quad \forall \ell \in \{0, 1, \ldots, 12\} \qquad (41)$$

The UT is now applied to the propagated sigma points, determining the error covariance at time t_k, with

$$C_{i,j}^-(t_k) = \frac{1}{n + \lambda} \left\{ \lambda \Big[\chi_0(t_k) - \delta x_{i,j}^-(t_k) \Big] \Big[\chi_0(t_k) - \delta x_{i,j}^-(t_k) \Big]^T \right.$$
$$\left. + \frac{1}{2} \sum_{\ell=1}^{12} \Big[\chi_\ell(t_k) - \delta x_{i,j}^-(t_k) \Big] \Big[\chi_\ell(t_k) - \delta x_{i,j}^-(t_k) \Big]^T \right\} \qquad (42)$$

C. Maneuver Determination

The unknown maneuver is determined by combining the recursive likelihood estimation method of Sec. III.A and the relative state propagation of Sec. III.B. This method is designed to target low-thrust maneuvers that can be regarded as instantaneous changes in velocity and therefore modeled as a three-dimensional vector. According to the notation introduced in Sec. III.A, the true (unknown) maneuver is denoted as ΔV and its estimate is $\hat{\theta}$, and the true (unknown) time of execution as t_m and its estimated value is $\hat{\tau}$. The time of the maneuver is first determined, enabling the subsequent estimation of the direction and magnitude.

The maneuver detection algorithm is based on principles of MMAE. With MMAE, the likelihood of each hypothesis given the observation history is used to determine the most likely system model—in this case the maneuver time and magnitude direction. Both maximum *a posteriori* and weighted sums can be used to interpret the MMAE results to determine the estimated hypotheses [33]. In general, maximum *a posteriori* interpretations result when the set of hypotheses is discrete and weighted sums are more appropriate for continuous-valued hypotheses.

For this work, a combination of maximum *a posteriori* and weighted sum interpretations is used. Specifically, the maneuver time estimate is determined as a maximum *a posteriori* estimate, and the maneuver magnitude and direction via a weighted sum. This mixed interpretation is used because of the nature in which hypotheses are generated. Specifically, maneuver magnitude and direction hypotheses are generated at each discrete maneuver time, and therefore the propagated states are inherently conditional on the hypothesized maneuver times. After first identifying the maneuver time, the magnitude and direction, having been sampled from a continuous distribution for a given maneuver time, can be aggregated using the weighted sum. In contrast, if the first time was aggregated via a weighted sum, then no such hypotheses would exist in the maneuver

magnitude/direction that are reflective of a maneuver having occurred at the estimated time.

1. Time Estimation

The estimated time of execution of the maneuver is given by the time with the highest computed likelihood, given a sequence of observations, i.e., the maximum *a posteriori* estimate. If a finite set Θ_M approximating the set of available maneuvers at any given time $\tau_i \in T_{\Delta t_s}$ is defined as in Sec. II, then, by the law of total probability, the maneuvering time can be determined as

$$\hat{\tau} \equiv \underset{i \in \{0, \ldots, K+1\}}{\operatorname{argmax}} P(\tau_i | \mathcal{Y}_k) = \underset{i \in \{0, \ldots, K+1\}}{\operatorname{argmax}} \sum_{j=1}^M P(\tau_i, \theta_j | \mathcal{Y}_k) \qquad (43)$$

where $P(\tau_i, \theta_j | \mathcal{Y}_k)$ is the conditional probability given by Eq. (13). The sum of probabilities in Eq. (43) is denoted as $S_i \equiv \sum_{j=1}^M P(\tau_i, \theta_j | \mathcal{Y}_k)$. The conditional probability has been derived in such a manner that the final expression is recursive in the measurements, meaning that each new observation enables a new estimation of $\hat{\tau}$. This feature is exploited to achieve better estimates. Note that $\hat{\tau}$ is selected from the discretized set $T_{\Delta t_s}$, and hence the choice of Δt_s will affect the resolution and thus the accuracy of the estimate.

2. Direction and Magnitude Estimation

The direction and magnitude of ΔV are determined after the time estimate $\hat{\tau}$ is available. The likelihoods $P(y_k | x_{i,j}^-(t_k))$ computed for every sampled maneuver $\theta_j \in \Theta_M$ at time $\hat{\tau}$ are gathered, and used as weights to calculate the vector estimate $\hat{\theta}$. Let the weights be defined such that $w_j(t_k) \equiv P(\hat{\tau}, \theta_j | \mathcal{Y}_k)$ and $w_j(t_{k-1}) \equiv P(\hat{\tau}, \theta_j | \mathcal{Y}_{k-1})$. A recursive formulation for the weights is given by

$$w_j(t_k) = P\Big(y_k | x_{i,j}^-(t_k)\Big) w_j(t_{k-1}), \;\; \forall j \in \{1, \ldots, M\} \qquad (44a)$$

$$w_j(t_k) \leftarrow \frac{w_j(t_k)}{\displaystyle\sum_{j \in \{1, \ldots, M\}} w_j(t_k)} \qquad (44b)$$

where $\hat{\imath} \equiv \min_i[|\hat{\tau} - \tau_i| : i \in \{0, \ldots, K+1\}]$. The estimated maneuver is computed as a weighted sum of the hypothesized values:

$$\hat{\theta} = \sum_{j \in \{1, \ldots, M\}} w_j(t_k)\theta_j \qquad (45)$$

Also, the associated error covariance is given by

$$C_\theta = \sum_{j \in \{1, \ldots, M\}} w_j(t_k)\Big(\theta_j - \hat{\theta}\Big)\Big(\theta_j - \hat{\theta}\Big)^T \qquad (46)$$

3. State Estimation

The states at the time of each new observation can be estimated in a similar fashion by first computing the weight-averaged perturbation:

$$\delta \hat{x}^+(t_k) = \sum_{j \in \{1, \ldots, M\}} w_j(t_k)\delta x_{\hat{\imath},j}(t_k) \qquad (47a)$$

$$\hat{x}^+(t_k) = x_n(t_k) + \delta \hat{x}^+(t_k) \qquad (47b)$$

with error covariance matrix given by

$$C^+(t_k) = \sum_{j \in \{1, \ldots, M\}} w_j(t_k)\big(\delta x_{\hat{\imath},j}(t_k) - \delta \hat{x}^+(t_k)\big)\big(\delta x_{\hat{\imath},j}(t_k) - \delta \hat{x}^+(t_k)\big)^T \qquad (48)$$

This enables the direct estimation of the states at the time of the last observation.

4. MD Algorithm

For completeness, the full algorithm to determine the most likely maneuver at each new observation is summarized as Algorithm 1. Note that when computing the likelihood for the first observation after maneuvering, i.e., $y_1 \equiv y(t_1)$, the prior probability can be initialized as in Eq. (9), i.e., $P(\tau_i, \theta_j | \mathcal{Y}_0) = P(\tau_i, \theta_j)$. The prior probability before any observation has been made is, therefore, uniform (if there is no additional information to give a better initial guess).

Algorithm 1: Recursive likelihood estimation of maneuver and execution time

---

Parameter: time-step size $\Delta t_s > 0$, number of maneuver samples per time step $M > 0$

Input: nominal trajectory $x_n(t) = \{r_n(t), \dot{r}_n(t)\}$ and error covariance $C_n(t)$ from EKF $\forall\ t \in [t_0, t_k]$, previously computed likelihood $P(\tau_i, \theta_j | \mathcal{Y}_{k-1})$, new measurement y_k, time t_k, and process G and noise R covariances.

Output: maneuver $\hat{\theta}$, error covariance C_θ, and execution time $\hat{\tau}_m$ estimation

1 Generate set of times until the time of first observation
$T_{\Delta t_s} \equiv \{t_0, t_0 + \Delta t_s, \ldots, t_0 + K\Delta t_s\}$,

2 Generate random set of maneuvers $\Theta_M \equiv \{\theta_1, \ldots, \theta_M\}$,

3 **for** $i \in \{0, \ldots, K\}$ **do**

4   Compute $\Phi(t_k, \tau_i)$ with Eq. (31) or Eq. (39),

5   **for** $j \in \{1, \ldots, M\}$ **do**

6   Define the velocity deviation $\delta x_{i,j}(\tau_i) = [0^T\ \theta_j^T]^T$,

7   Propagate to measurement time $\delta x_{i,j}^-(t_k) = \Phi(t_k, \tau_i)\delta x_{i,j}(\tau_i)$,

8   Compute absolute position $x_{i,j}^-(t_k) = x_n(t_k) + \delta x_{i,j}(t_k)$,

9   Compute error covariance $C_{i,j}^-(t_k)$ using Eq. (34) or Eq. (42),

10   Compute $P(y_k | x_{i,j}^-(t_k))$ using Eq. (14),

11   Compute $P(\tau_i, \theta_j | \mathcal{Y}_k)$ using Eq. (13),

12   Compute $S_i = \sum_{j \in \{1, \ldots, M\}} P(\tau_i, \theta_j | \mathcal{Y}_k)$,

13 Normalize $P(\tau_i | \mathcal{Y}_k) = S_i / \sum_{i \in \{0, \ldots, K\}} S_i$,

14 Compute $\hat{\tau}$ using Eq. (43)

15 Compute $\hat{\theta}$ and C_θ using $\hat{\tau}$, Eqs. (45) and (46).

In practice, some steps of Algorithm 1 can be simplified to reduce memory and computation without severely compromising the accuracy of the method. For instance, the computation of the error covariance $C_{i,j}^-(t_k)$, in Step 9, might differ very little from the nominal error covariance $C_n(t_k)$ obtained in the EKF. In some cases, especially if Eq. (42) is employed, it might be beneficial to assume that $C_{i,j}^-(t_k) = C_n(t_k)$.

IV. Simulation Results

Results for the proposed MD algorithm are presented in the form of numerical simulations. Two scenarios are studied: the maneuver of a near-Earth spacecraft, for which the main results are obtained and discussed, and a cislunar case demonstrating the effectiveness of the general procedure introduced in Sec. III.B.2. It is important to note that there may exist more than one maneuver time and magnitude that results in the same orbit once the object is seen again. The goal of the simulation results is to choose enough sensor observations so that the highest probability is given to the true maneuver time. This obviously varies depending on the type of maneuver.

Algorithm 1 is impacted by multiple parameters; some of these parameters can be thought of as tunable, but a proper parameter setup will highly depend on the statistical information and physical knowledge available. Some of these quantities, such as the minimum and maximum allowed magnitudes ($\theta_{\min}$ and $\theta_{\max}$) in the maneuver search space Θ_M, the time at which observations are

received, and the covariances of the dynamic model and the observations, are analyzed further in this section based on numerical simulations of both the near-Earth and cislunar scenarios.

The parameter values to generate the results are presented for each scenario. The system model in Eq. (1) is then simulated using Euler–Maruyama integration, and a maneuver is scheduled to be executed in the simulation at a specific time t_m. By means of a sequence of a few observations, the results show how the algorithm estimates the time of execution and the change in the relevant components of the velocity vector caused by the maneuver.

A. Near-Earth Scenario

The first scenario is that of a near-Earth spacecraft. The initial position and velocity vectors are given by Eq. (49), which corresponds to a semimajor of 6928.137 km and an eccentricity of 0.05:

$$r_n(t_0) = \begin{bmatrix} 6584.73 \\ 0 \\ 0 \end{bmatrix} \text{km}, \quad \dot{r}_n(t_0) = \begin{bmatrix} 0 \\ 7.9743 \\ 0 \end{bmatrix} \frac{\text{km}}{\text{s}} \quad (49)$$

Two measurement collection strategies are considered, as shown in Fig. 3. The first considers that only three observations are collected 30 minutes apart, while the second uses a burst collection of six observations each 1 minute apart. In both cases, the simulated maneuvered satellite is first observed after 4.5 hours since the beginning of the simulation. The set of observations is generated based on the simulations by adding noise to the state vectors, as described by the system model in Eq. (1) and the dynamics g_E.

The following error covariance of the state vector at time t_0 is used:

$$C_{\text{TNH}}(t_0) = \begin{bmatrix} C_r & 0_3 \\ 0_3 & C_v \end{bmatrix} \quad (50)$$

with submatrices C_r and C_v defined as

$$C_r = \begin{bmatrix} 1.5 \cdot 10^3 & 0 & 0 \\ 0 & 5 \cdot 10^2 & 0 \\ 0 & 0 & 5 \cdot 10^2 \end{bmatrix} \text{m}^2 \quad (51)$$

$$C_v = \begin{bmatrix} 4.44 \cdot 10^{-6} & 0 & 0 \\ 0 & 0.1 \cdot 10^{-4} & 0 \\ 0 & 0 & 0.1 \cdot 10^{-4} \end{bmatrix} \frac{\text{m}^2}{\text{s}^2} \quad (52)$$

Note that the error covariance matrix $C_{\text{TNH}}(t_0)$ is expressed here in the tangential-normal-out-of-plane (TNH) frame, instead of the ECI frame, to ease the interpretation of the values. The TNH frame is defined by the following basis:

$$\text{TNH} := \left\{ \frac{\dot{r}_n}{\|\dot{r}_n\|}, \frac{\ell \times \dot{r}_n}{\|\ell \times \dot{r}_n\|}, \frac{\ell}{\|\ell\|} \right\} \quad (53)$$

Similarly, the stochastic process and the observations are affected by Gaussian noise with diffusion and covariance matrices (expressed in the ECI frame) given by

$$\Sigma = \begin{bmatrix} 0_3 & 0_3 \\ 0_3 & I_3 \cdot 10^{-6}\ \frac{\text{m}^2}{\text{s}^3} \end{bmatrix} \quad (54a)$$

$$R = 10^3 \cdot I_3\ \text{m}^2 \quad (54b)$$

In order to test Algorithm 1, it is convenient to also consider two situations: one where a conservative search space $\tilde{\Theta}$ is defined, representing a complete lack of information about the magnitude
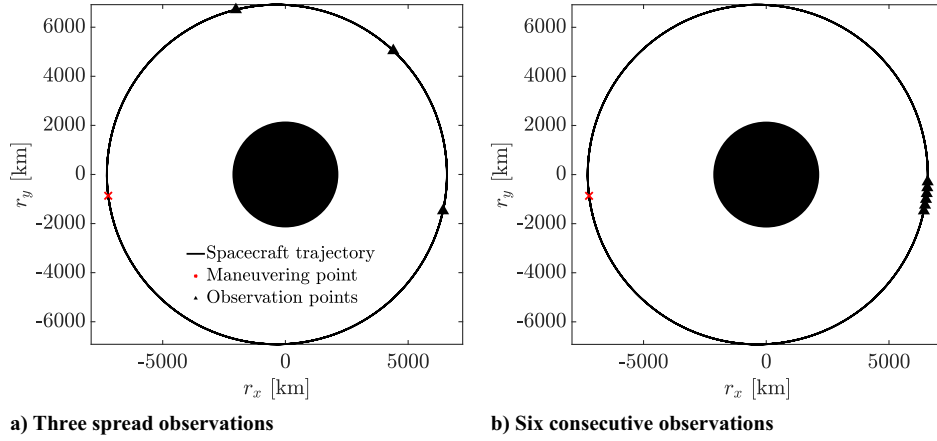
a) Three spread observations   **b) Six consecutive observations**

Fig. 3 Two near-Earth scenarios.

of the maneuver, and another one where some information is available, which allows for the reduction of the search space. The minimum and maximum magnitude values of the maneuver are then considered to be $\theta_{\min} = 0$ m/s and $\theta_{\max} = 0.7$ m/s for the former situation, and $\theta_{\min} = 0$ m/s and $\theta_{\max} = 0.3$ m/s for the latter, whereas the actual simulated maneuver has a magnitude of $\|\Delta V\| = 0.2$ m/s. Finally, the discretization parameters are defined to be $\Delta t_s = 10$ s and $M = 10^4$ particles. It is important to note that the true maneuver time is not within the models of the MMAE filter, which further stresses the algorithm. Also, the step size has been chosen so that the maneuver reconstruction is not affected by the maneuver time not being within the MMAE filter bank. The true maneuver vector ΔV_{TNH} and time of execution for the maneuver t_m are

$$\Delta V_{\mathrm{TNH}}(t_m) = [-0.1724 \ \ 0.1014 \ \ 0]^T \ \frac{\mathrm{m}}{\mathrm{s}} \qquad (55\mathrm{a})$$

$$t_m = 0.83 \ \mathrm{h} \qquad (55\mathrm{b})$$

The posterior probabilities $P(\tau_i | \mathcal{Y}_k)$ obtained for a sequence of 1, 2, and 3 observations (each taken 30 minutes apart) and with the two different upper bounds on $\tilde{\Theta}$ can be found in Fig. 4. Both cases share the same initial error covariance, as defined in Eq. (50). The red dashed line indicates the true time of execution of the maneuver. The plots in Fig. 4 illustrate a fast and accurate convergence of the posterior probability $P(\tau_i | \mathcal{Y}_k)$ around the true time of execution of the maneuver after the three observations, provided a good statistical description of the system. These results also show how a tighter searching space, Fig. 4b, converges faster than when a conservative searching space is considered, Fig. 4a.
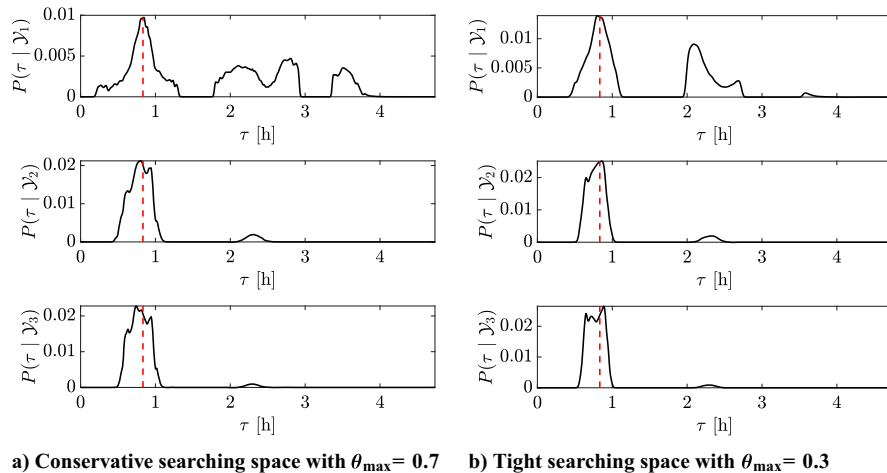
A different effect is achieved when multiple observations are collected at a higher cadence, as shown in Fig. 5. As compared to Fig. 4, convergence to the true maneuver time is slower on a per-observation basis, which is an expected result since deviations will spread less as the time between observations is less, as depicted in Fig. 6. Moreover, decreasing the searching space does not seem to improve the convergence of the algorithm in this case. Nevertheless, the algorithm does show a reduction of the variance of the posterior distribution quite effectively.

In order to understand the limitations of Algorithm 1, the initial error covariance $C_{\mathrm{TNH}}(t_0)$ and the measurement noise covariance R are increased to be given by

$$C_r = \begin{bmatrix} 15 & 0 & 0 \\ 0 & 5 & 0 \\ 0 & 0 & 5 \end{bmatrix} \cdot 10^3 \ \mathrm{m}^2 \qquad (56)$$

$$C_v = \begin{bmatrix} 4.44 & 0 & 0 \\ 0 & 100 & 0 \\ 0 & 0 & 100 \end{bmatrix} \cdot 10^{-7} \ \frac{\mathrm{m}^2}{\mathrm{s}^2} \qquad (57)$$

$$R = (5 \cdot 10^3) \ I_3 \ \mathrm{m}^2 \qquad (58)$$

Results for this case can be found in Fig. 7 for a sequence of three observations, each taken 30 minutes apart, and two different upper bounds on $\tilde{\Theta}_M$.

The increase in noise results in degradation compared to the results in Fig. 4. On the one hand, it allows particles that deviate
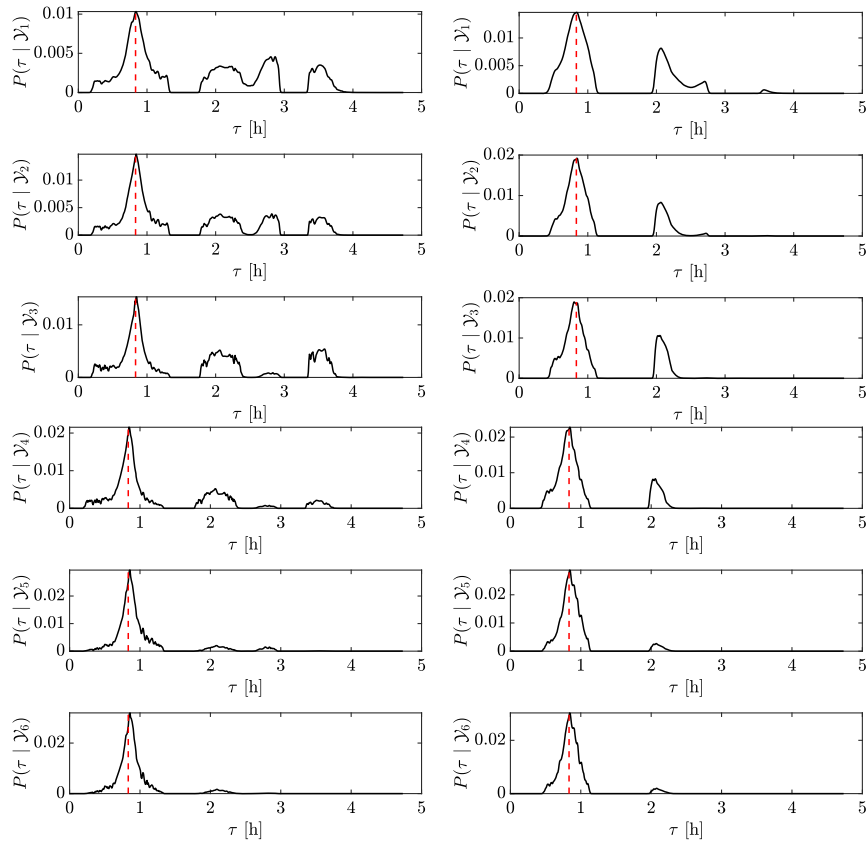
a) Conservative searching space with $\theta_{\max} = 0.7$ **b) Tight searching space with $\theta_{\max} = 0.3$**

Fig. 4   Near-Earth scenario with three spread observations and small error covariances.

a) **Conservative searching space with θ_{max}= 0.7**   b) **Tight searching space with θ_{max}= 0.3**

Fig. 5   Near-Earth scenario with six consecutive observations and small error covariances.
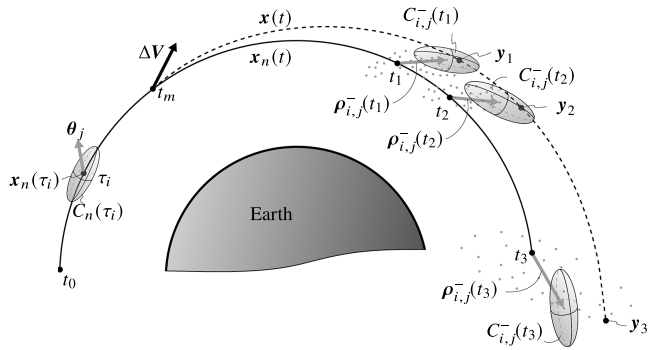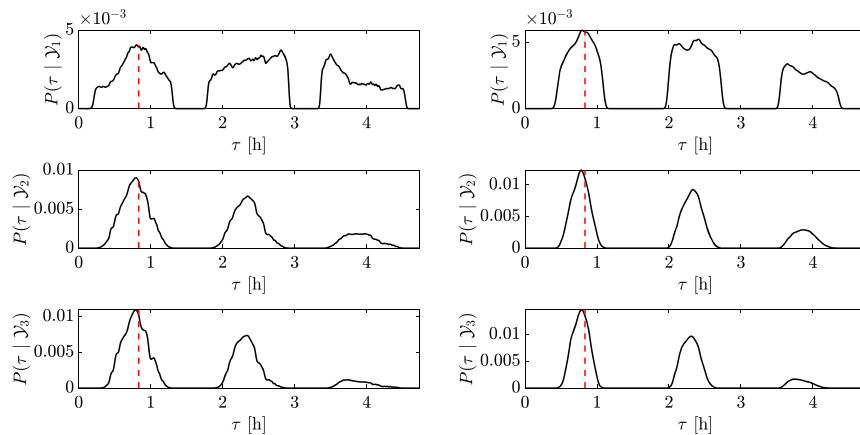

Fig. 6   Propagation of an arbitrary maneuver with two observations close to each other and one observation far from the previous two.
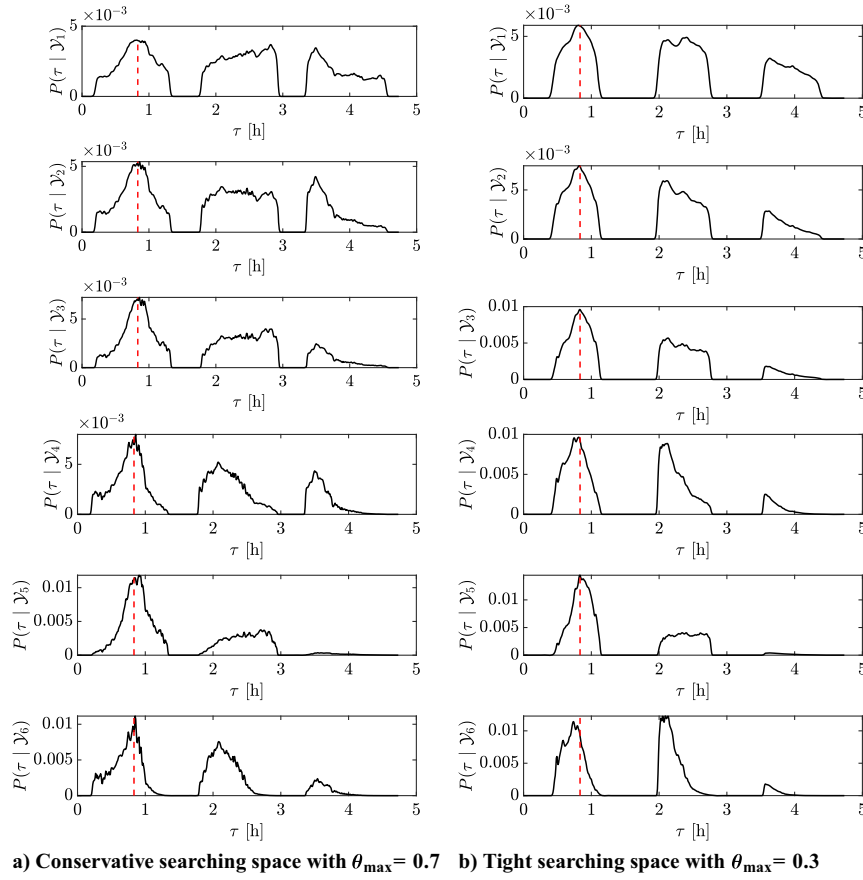
further from the measurements to contribute to the posterior probability, leading to an increase in variances and a slower convergence rate. Reducing the search space improves the results, as the variance decreases and the posterior probability around the truth increases with $\theta_{max} = 0.3$, compared to the results obtained with $\theta_{max} = 0.7$.

The results for the six consecutive observations with time gaps of 1 minute are shown in Fig. 8. In this case, the algorithm fails to eliminate other possible solutions more effectively, as multiple values of τ_i share similar values in the peaks of the posterior probability. Decreasing the upper bound θ_{max} from 0.7 to 0.3, as shown in Fig. 8b, reduces the variance of the posterior probability but still fails to eliminate other likely solutions for the timing of the maneuver. Notably, the time differences between the peaks of the posterior probability roughly coincide with the orbital period. It becomes clear that, in this simulated case, three orbits are spanned in

a) **Conservative searching space with θ_{max}= 0.7**   b) **Tight searching space with θ_{max}= 0.3**

Fig. 7   Near-Earth scenario with three spread observations and large error covariances.

a) **Conservative searching space with** $\theta_{max}= 0.7$ b) **Tight searching space with** $\theta_{max}= 0.3$

Fig. 8 **Near-Earth scenario with six consecutive observations and large error covariances.**

the time interval between t_0 and the first measurement at t_1. Finally, it is worth noting that, from one observation to another (e.g., from observation 5 to observation 6), times with little prior probability can reappear as more probable after the new observation. This phenomenon, also observed between observations 3 and 4, is likely caused by observation noise errors and the short intervals between consecutive observations.

1. Monte Carlo Campaign 1: Fixed Low-Thrust Maneuver and Random Observations

To study the accuracy of the maneuver time $\hat{\tau}$ and vector $\hat{\boldsymbol{\theta}}$ estimates as a function of the observations, a Monte Carlo (MC) analysis is conducted. To that end, three spread measurements are randomly taken in each simulation with observational time gaps between 30 minutes and 1 hour. The error covariances employed for the entire MC campaign are given in Eqs. (51), (52), and (54). A total of 1000 simulations are performed, for which the posterior probability $P(\tau_i|\mathcal{Y}_k)$ is determined as has been shown above, and the value of $\hat{\tau}$ with maximum a posteriori probability is taken as the estimate of t_m (MAP estimate). The maneuver vector estimate $\hat{\boldsymbol{\theta}}$ is obtained for those times $\hat{\tau}$ using Eq. (44).

The posterior probabilities $P(\tau_i|\mathcal{Y}_k)$ for each Monte Carlo (MC) realization are shown as gray lines in Fig. 9. This represents the probability of a maneuver occurring at a time $t \in [t_0, t_1]$, given the first, second, and third observations. The blue shaded area represents 98% of the realizations (ranging from the 1st to the 99th percentile) where the algorithm successfully isolated the correct solution, and the dashed line indicates the median.

According to the posterior probabilities obtained in Fig. 9, the estimated times and maneuvers are estimated for each realization and depicted in Figs. 10 and 11, together with the true time (red dashed line) and the true maneuver vector ΔV (red cross). Only two axes are shown in Fig. 11, since the true maneuver is assumed to have only in-track and radial components. As seen, the in-track component is accurately estimated, while the radial component
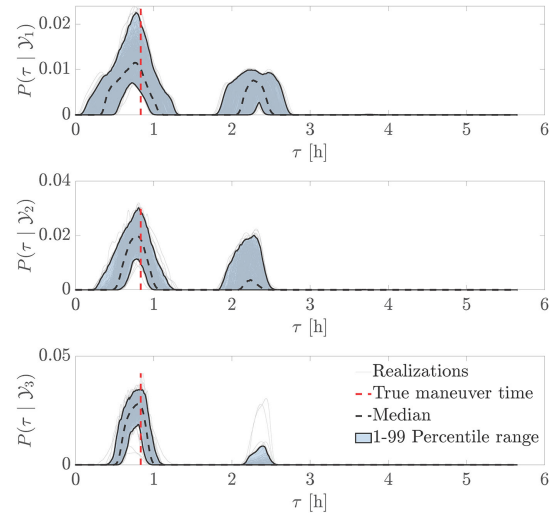
Fig. 9 **Posterior probabilities after 1, 2, and 3 observations in the Monte Carlo campaign.**

exhibits larger variance and has a mean close to zero. This is likely because the radial direction is less sensitive to changes in the spacecraft's momentum, especially for impulsive maneuvers of small magnitude, as the one at hand.

The relative trajectories on the plane of the maneuver, with respect to the nominal orbit, are reconstructed based on the estimates for $\hat{\tau}$ and $\hat{\boldsymbol{\theta}}$. The relative trajectory error of each realization is shown as a gray line in Fig. 12, with the true perturbed trajectory represented by the x-axis. The orange area represents 98% of the realizations (ranging from the 1st to the 99th percentile). The median, shown as the black dashed line, is almost aligned with the x-axis.
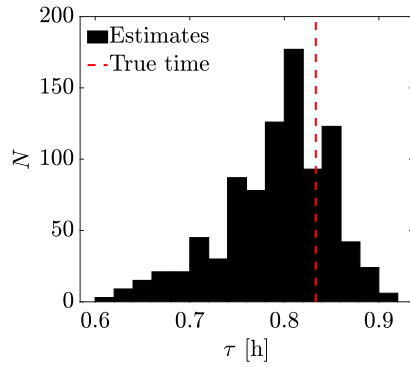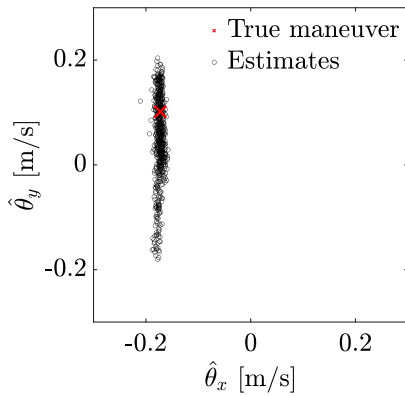
Fig. 10　Estimated times in the MC campaign.
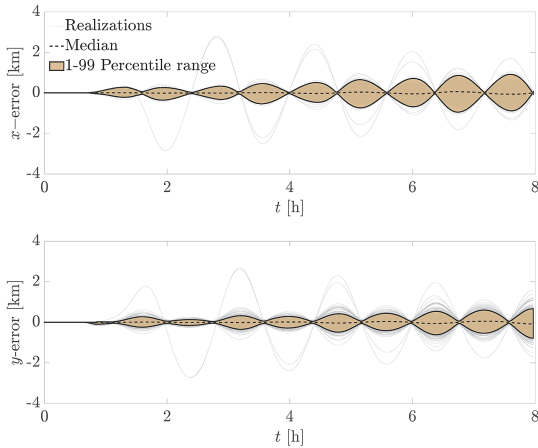

Fig. 11　Estimated maneuvers in the MC campaign.
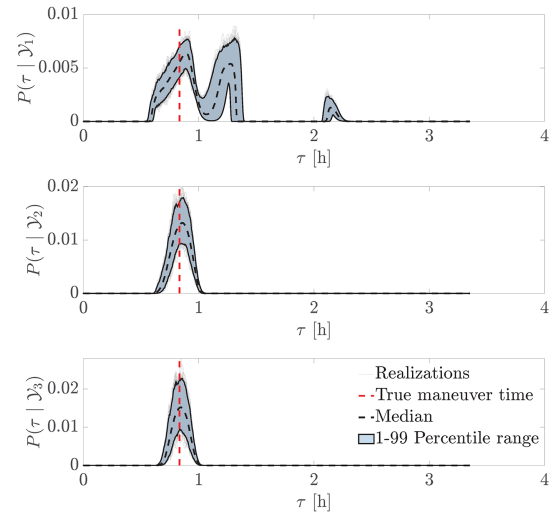

Fig. 12　Error of the estimated trajectory in the MC campaign.

Fig. 13　Posterior probabilities after 1, 2, and 3 observations in the Monte Carlo campaign.

Fig. 14　Estimated times in the MC campaign.

2.　Monte Carlo Campaign 2: Fixed High-Thrust Maneuver and Random Observations

A second Monte Carlo campaign is performed to explore the extent of the validity of the STM. This MC campaign near Earth involves a large-magnitude maneuver that can provide phasing-type maneuvers, which are routinely done by spacecraft. As before, a total of 1000 realizations are considered for which the posterior probability $P(\tau_i|\mathcal{Y}_k)$ is determined. The value of $\hat{\tau}$ with maximum probability is taken as the estimate of t_m (MAP estimate). For this case, the total simulated time and the time of the maneuver are maintained. The maneuver vector is, however, increased such that

$$\Delta \boldsymbol{V}_{\text{TNH}}(t_m) = [10 \ 5 \ 0]^T \ \frac{\text{m}}{\text{s}} \tag{59a}$$

$$t_m = 0.83 \ \text{h} \tag{59b}$$
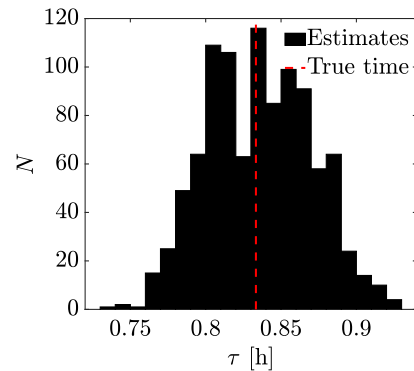
The search space for the maneuver vector is changed accordingly to have a lower bound $\theta_{\min} = 5$ m/s and an upper bound $\theta_{\max} = 15$ m/s.

Large maneuvers quickly separate the maneuvering spacecraft from the nominal trajectory, which has both advantages and drawbacks in this type of analysis. On the one hand, the algorithm might converge with fewer observations taken during a shorter period. For instance, in Fig. 13, the posterior probabilities for this Monte Carlo run show a clear concentration around the true time already after the second observation. Despite the randomization, all the cases with observations taken soon after the maneuver have effectively converged, as well as those cases where observations were taken long after the maneuver. As a consequence, the final maneuver time estimate, shown in Fig. 14, exhibits a reduction in variance compared to the low-thrust case shown in Fig. 10. However, the accuracy of the first-order approximation (the STM) drops with larger relative distances between the nominal and maneuvered trajectory, thus becoming a limiting factor for the accurate estimation of the maneuver if the object remains unobserved for periods of time where large relative distances are allowed to occur.

Although the execution time of the maneuver has been successfully identified in all realizations after the second observation, also showing a smaller variance than in the low-thrust MC campaign, the estimated maneuver begins to exhibit a small bias in the in-track component, as seen in Fig. 15. This artifact is a direct effect of the drop in accuracy of the STM discussed in the previous paragraph. Since all the particles exhibit the same in-track bias, this suggests that the accuracy would not be improved by increasing the number of particles but rather by increasing the domain of accuracy of the propagation method, e.g., using higher-order state transition tensors
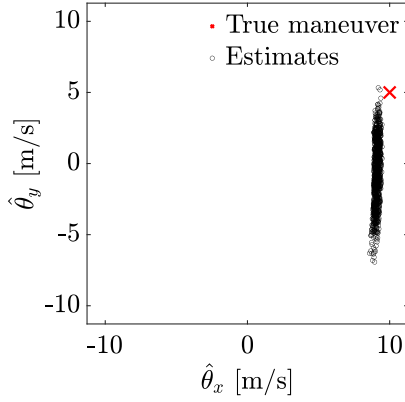
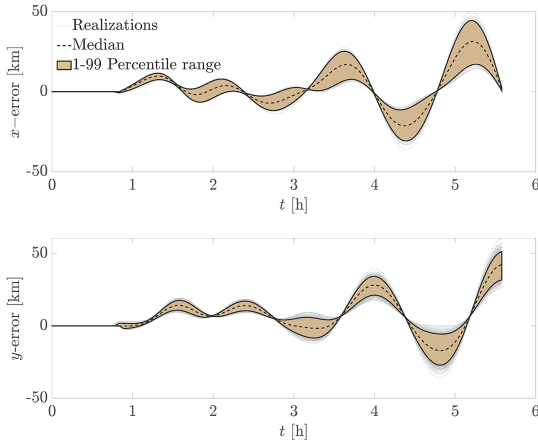**Fig. 15   Estimated maneuvers in the MC campaign.**

Fig. 16   Error of the estimated trajectory in the MC campaign.

(STTs). Provided that the dynamics are largely affected by the in-track component of the maneuver, the small error in the estimation of that component is enough to cause the errors witnessed in Fig. 16, compared to the small-thrust maneuver case.

3.   Monte Carlo Campaign 3: Random Low-Thrust Maneuvers and Fixed Observations

A third and final Monte Carlo campaign is presented here for the near-Earth case, where the true maneuvers are random in terms of both time and vector. In contrast, the maneuvered spacecraft is now observed at three fixed times: the first observation occurs 6 hours after the start of the simulation, with the subsequent observations spaced 1 hour apart. The true maneuvers satisfy

$$0 < \|\Delta \boldsymbol{V}_{\mathrm{TNH}}(t_m)\| \le 0.2 \; \frac{\mathrm{m}}{\mathrm{s}}, \quad \text{with } \Delta \boldsymbol{V}_{\mathrm{TNH},z}(t_m) = 0 \quad (60\mathrm{a})$$

$$0 \le t_m \le 2 \; \mathrm{h} \quad (60\mathrm{b})$$

where $\Delta \boldsymbol{V}_{\mathrm{TNH},z}$ is the out-of-plane component of the vector. The maneuver search space remains as in the low-thrust case. The results of this campaign are shown in Fig. 17, which presents the errors of the estimators $\hat{\tau}$ and $\hat{\boldsymbol{\theta}}$. These figures demonstrate that the method is capable of accurately estimating the timing of maneuvers occurring at different points in the orbit, as well as the relevant components of the maneuver vector (i.e., the in-track component).

B.   Cislunar Scenario

A second scenario considers a ballistic return trajectory from the moon toward Earth, with a correcting in-track maneuver. The trajectory is depicted in Fig. 18, with the red cross indicating the point on the trajectory where the maneuver is executed. The black triangles indicate the points where the different observations of the spacecraft are taken.

The mean initial conditions for the cislunar trajectory case are summarized in the following vectors, expressed in nondimensional units (ud and ut for distance and time, respectively):

$$\boldsymbol{r}(t_0) = \begin{bmatrix} 1.2 \\ 0 \\ 0 \end{bmatrix} \mathrm{ud}, \quad \dot{\boldsymbol{r}}(t_0) = \begin{bmatrix} 0 \\ -1.05 \\ 0 \end{bmatrix} \frac{\mathrm{ud}}{\mathrm{ut}} \quad (61)$$
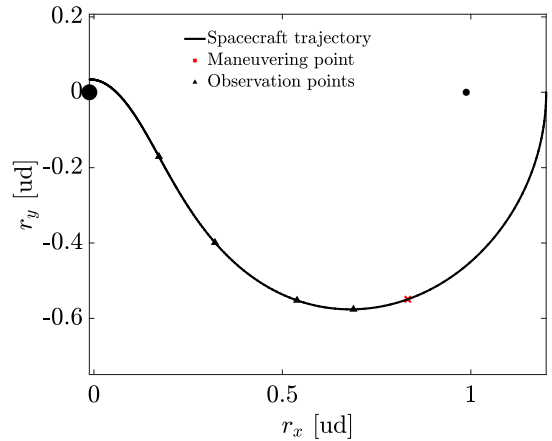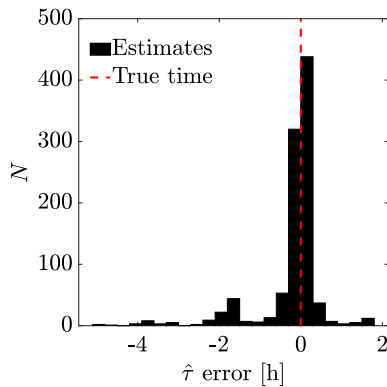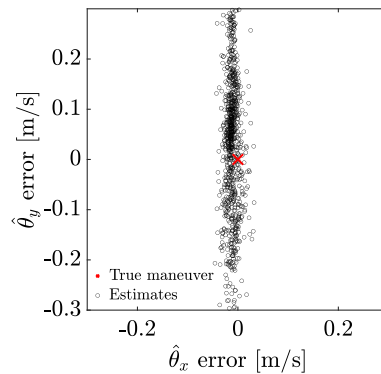

Fig. 18   Cislunar trajectory.

a) Histogram based on the estimation errors of t_m

b) Scatter plot based on the estimation errors of ΔV

Fig. 17   Estimation errors in the MC campaign with random maneuvers and fixed observation times.

The following error covariance matrix is expressed in the local frame of reference in nondimensional units:

$$C_L(t_0) = \begin{bmatrix} C_r & 0_3 \\ 0_3 & C_v \end{bmatrix} \tag{62}$$

with submatrices

$$C_r = \begin{bmatrix} 0.65 & 0 & 0 \\ 0 & 16.3 & 0 \\ 0 & 0 & 0.65 \end{bmatrix} \cdot 10^{-9} \text{ ud}^2 \tag{63a}$$

$$C_v = \begin{bmatrix} 0.38 & 0 & 0 \\ 0 & 0.096 & 0 \\ 0 & 0 & 0.096 \end{bmatrix} \cdot 10^{-13} \frac{\text{ud}^2}{\text{ut}^2} \tag{63b}$$

where the local frame is defined here using the angular momentum vector of the Earth–moon system ℓ_{EM} as

$$L := \left\{ \frac{\dot{r}_n}{\|\dot{r}_n\|}, \frac{\ell_{EM} \times \dot{r}_n}{\|\ell_{EM} \times \dot{r}_n\|}, \frac{\ell_{EM}}{\|\ell_{EM}\|} \right\} \tag{64}$$

The previous error covariance is not determined from experimental data. Note that uncertainty models in cislunar space remain to be accurately studied and lack proper characterization. The stochastic process and the observations are again affected by Gaussian noise with diffusion and covariance matrices (expressed in the synodic frame) given by

$$\Sigma = \begin{bmatrix} 0_3 & 0_3 \\ 0_3 & 10^{-12} \cdot I_3 \frac{\text{ud}^2}{\text{ut}^2} \end{bmatrix} \tag{65a}$$

$$R = \left(0.163 \cdot 10^{-9} \right) I_3 \text{ ud}^2 \tag{65b}$$

Once again, Algorithm 1 is tested with two different bounds on the searching space $\tilde{\Theta}$: a conservative one, with a minimum bound on the magnitude of 1 cm/s, i.e., $\theta_{\min} = 9.84 \cdot 10^{-6}$ in nondimensional units, and a maximum magnitude of slightly above 2 m/s, i.e., $\theta_{\max} = 0.00216$, and a tight searching space around the actual magnitude of the maneuver, which has bounds $\theta_{\min} = \|\Delta V\| - 10^{-3}$ and $\theta_{\max} = \|\Delta V\| + 10^{-3}$. The discretization parameters remain unchanged, being $\Delta t_s = 10$ s and $M = 10^4$ particles. The results are obtained for a 2 m/s maneuver vector ΔV in the in-track direction, for which the description in the synodic (inertial)

frame and a time of execution in nondimensional units are given by

$$\Delta V_{\text{SYN}}(t_m) = [-18.54 \cdot 10^{-4} \quad -6.599 \cdot 10^{-4} \quad 0]^T \frac{\text{ud}}{\text{ut}} \tag{66a}$$

$$t_m = 0.7 \text{ ut} \tag{66b}$$

and a sequence of four observations taken at different times, as depicted in Fig. 18.

Figure 19 shows the fast and accurate convergence of the posterior $P(\tau_i|\mathcal{Y}_k)$ around the true time of execution of the maneuver, indicated by the red dashed line. It also illustrates how the convergence already occurs after the first observation when the searching space is tight around the magnitude of the maneuver. Note as well that the peak of the distribution shifts slightly toward the left with each new measurement, indicating that the STM is losing accuracy with every observation since they are quite far apart.

In order to understand the limitations of Algorithm 1, the initial error covariance $C(t_0)$ and the measurement noise covariance R are increased, as previously done in the near-Earth scenario, where now

$$C_r = \begin{bmatrix} 0.65 & 0 & 0 \\ 0 & 16.3 & 0 \\ 0 & 0 & 0.65 \end{bmatrix} \cdot 10^{-9} \text{ ud}^2 \tag{67a}$$

$$C_v = \begin{bmatrix} 0.38 & 0 & 0 \\ 0 & 0.096 & 0 \\ 0 & 0 & 0.096 \end{bmatrix} \cdot 10^{-13} \frac{\text{ud}^2}{\text{ut}^2} \tag{67b}$$

$$R = (0.65 \times 10^{-9}) I_3 \text{ ud}^2 \tag{67c}$$

These changes yield the results shown in Fig. 20 for the posterior probability $P(\tau_i|\mathcal{Y}_k)$ using the two different bounds on the searching space $\tilde{\Theta}$. It is clear that the variance of the posterior distribution increases drastically in both cases. Having a tight searching space reduces the overall uncertainty and rate of convergence.

1. Monte Carlo Campaign 4: Cislunar Case

A Monte Carlo campaign is once again carried out to study the precision of the estimators $\hat{\tau}$ and $\hat{\theta}$ as a function of the observations, which will now be distributed along the cislunar trajectory. The observations will be spread enough to ensure that they do not fall together in specific regions of the trajectory, especially close to the departure from the nominal trajectory, where the observations would provide very little information. The covariances used for the MC campaign are Eqs. (63a), (63b), and (65b). As before, a total of 1000
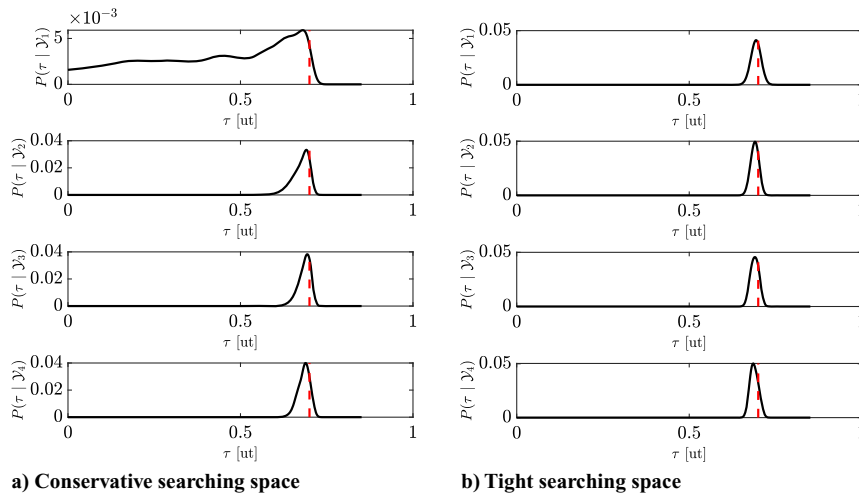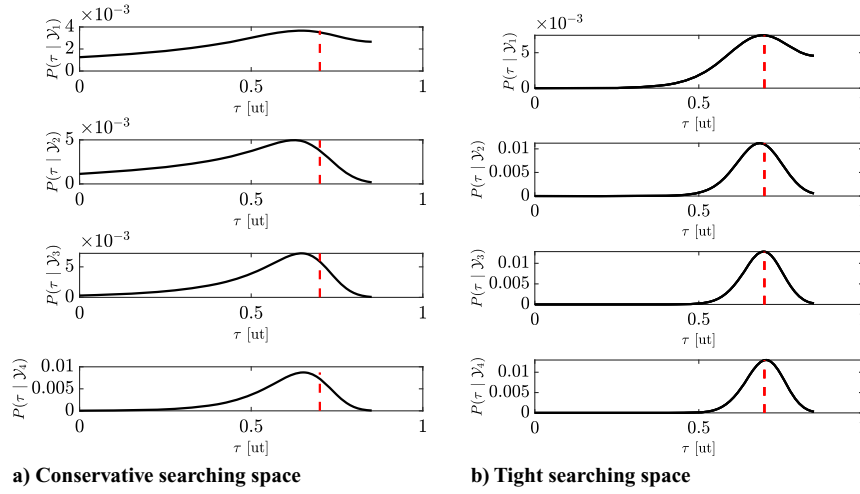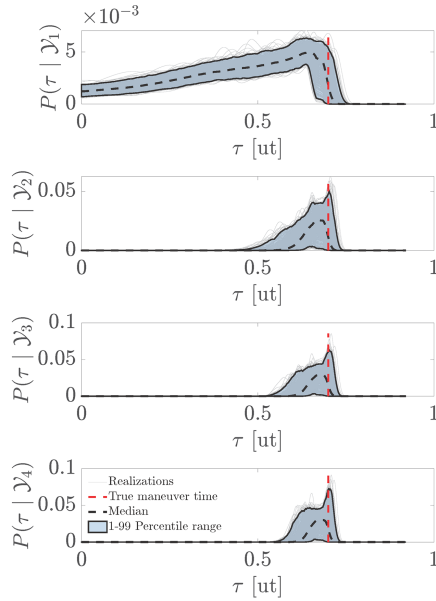

a) Conservative searching space   b) Tight searching space

Fig. 19   Posterior probabilities in the cislunar scenario with small initial error covariance.

Fig. 20 Posterior probabilities in the cislunar scenario with large initial error covariance.

simulations are performed, for which the posterior probability $P(\tau_i|\mathcal{Y}_k)$ is determined now using the numerical procedure to compute the STM. The value of $\hat{\tau}$ with maximum probability is taken as the estimate of t_m (MAP estimate). The maneuver vector estimate $\hat{\boldsymbol{\theta}}$ is obtained for those times $\hat{\tau}$ using the weighted sum in Eq. (44).
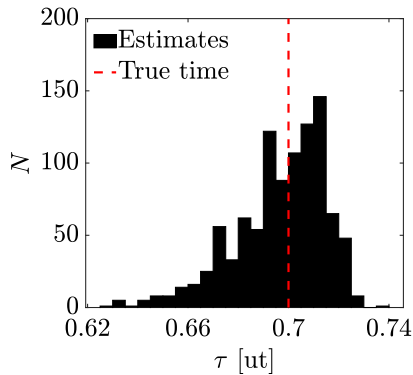
The results are shown in Figs. 21–24, demonstrating an accurate determination of the time and vector ΔV associated with the true maneuver. In this scenario, the trajectory is more sensitive to changes in momentum in both components, and the algorithm successfully identifies the magnitude of that change in both. The error of the estimated trajectories for each realization is shown in Fig. 24, expressed in kilometers. As seen, the largest error, which occurs close to the Earth's regime where nonlinear terms begin to influence the trajectory, remains below 100 km.

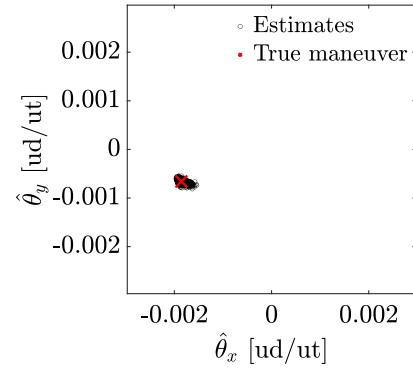
Fig. 21 Posterior probabilities after 1, 2, and 3 observations in the Monte Carlo campaign.

Fig. 23 Estimated maneuvers in the MC campaign.

Fig. 22 Estimated times in the MC campaign.
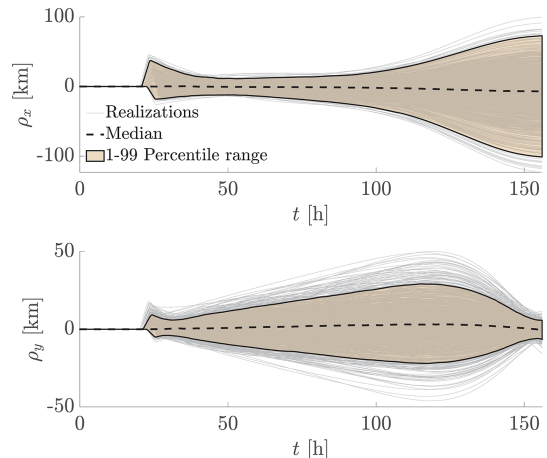
Fig. 24 Error of the estimated trajectory in the MC campaign.

V. Conclusions

This paper presents an algorithm for spacecraft maneuver determination. The algorithm combines multiple-model adaptive estimation with Bayes theorem to improve the accuracy of the maneuver estimates in a recursive manner based on new observations. Several advantages of the proposed method include accurate estimation of the maneuver time, as well as the estimation of maneuvers that occur well before the first observation is taken. The approach is computationally efficient, which can be readily parallelized for added efficiency, and can be employed not only for Earth-bounded trajectories but also in cislunar space and other nonlinear environments. The results presented in this paper show the efficacy of the algorithm and its capability of estimating the time, direction, and magnitude of a maneuver by using only a sequence of three observations taken 30 minutes apart, without any prior knowledge about the magnitude of the maneuver. The accuracy of the approach was demonstrated to be closely tied to the *a priori* uncertainty of the state estimates before the maneuver and the propagation model used. This analysis provides insight into the tracking systems where the approach can be employed. The approach in this paper relies on analytic first-order approximations through the use of state transition matrices (STMs), which provide computational efficiencies but may lose effectiveness when considering large time spans that prevent the omission of nonlinear dynamics and perturbation effects (such as *J*2). For these cases, numerically computed STMs or state transition tensors (STTs) can be employed, which increases the computational expense and provides better accuracy; however, the theory shown in this paper is unchanged.

References

[1] Linares, R., Vishwajeet, K., Singla, P., and Crassidis, J. L., "Information Theoretic Space Object Data Association Methods Using an Adaptive Gaussian Sum Filter," *AAS/AIAA Space Flight Mechanics Meeting*, American Astronautical Soc. Paper 11-148, Springfield, VA, 2011.

[2] Kalur, A., Szklany, S. A., and Crassidis, J. L., "Space Object Data Association Using Spatial Pattern Recognition Approaches," *Journal of the Astronautical Sciences*, Vol. 67, No. 4, 2020, pp. 1708–1734.
https://doi.org/10.1007/s40295-020-00217-0

[3] Crassidis, J. L., and Junkins, J. L., *Optimal Estimation of Dynamic Systems*, 2nd ed., CRC Press, Boca Raton, FL, 2012, Chaps. 3, 4.
https://doi.org/10.1201/b11154

[4] Goff, G. M., Black, J. T., and Beck, J. A., "Tracking Maneuvering Spacecraft with Filter-Through Approaches Using Interacting Multiple Models," *Acta Astronautica*, Vol. 114, Sept.–Oct. 2015, pp. 152–163.
https://doi.org/10.1016/j.actaastro.2015.05.009

[5] Jia, B., Blasch, E., Pham, K., Shen, D., Wang, Z., Tian, X., and Chen, G., "Space Object Tracking and Maneuver Detection via Interacting Multiple Model Cubature Kalman Filters," *IEEE Aerospace Conference Proceedings*, Vol. 2015, Inst. of Electrical and Electronics Engineers, Piscataway, NJ, 2015, pp. 1–8.
https://doi.org/10.1109/AERO.2015.7119076

[6] Kelecy, T., and Jah, M., "Detection and Orbit Determination of a Satellite Executing Low Thrust Maneuvers," *Acta Astronautica*, Vol. 66, No. 5, 2010, pp. 798–809.
https://doi.org/10.1016/j.actaastro.2009.08.029

[7] Magill, D. T., "Optimal Adaptive Estimation of Sampled Stochastic Processes," *IEEE Transactions on Automatic Control*, Vol. 10, No. 4, 1965, pp. 434–439.
https://doi.org/10.1109/TAC.1965.1098191

[8] Ko, H. C., and Scheeres, D. J., "Maneuver Detection with Event Representation Using Thrust Fourier Coefficients," *Journal of Guidance, Control, and Dynamics*, Vol. 39, No. 5, 2016, pp. 1080–1091.
https://doi.org/10.2514/1.G001463

[9] Huang, J., Hu, W., Xin, Q., and Du, X., "An Object Correlation and Maneuver Detection Approach for Space Surveillance," *Research in Astronomy and Astrophysics*, Vol. 12, No. 10, 2012, pp. 1402–1416.
https://doi.org/10.1088/1674-4527/12/10/003

[10] Worthy, J. L., Holzinger, M. J., and Scheeres, D. J., "An Optimization Approach for Observation Association with Systemic Uncertainty Applied to Electro-Optical Systems," *Advances in Space Research*, Vol. 61, No. 11, 2018, pp. 2709–2724.
https://doi.org/10.1016/j.asr.2018.02.041

[11] Lubey, D. P., and Scheeres, D. J., "Identifying and Estimating Mismodeled Dynamics via Optimal Control Policies and Distance Metrics," *Journal of Guidance, Control, and Dynamics*, Vol. 37, No. 5, 2014, pp. 1512–1523.
https://doi.org/10.2514/1.G000369

[12] Escribano, G., Sanjurjo-Rivo, M., Siminski, J. A., Pastor, A., and Escobar, D., "Automatic Maneuver Detection and Tracking of Space Objects in Optical Survey Scenarios Based on Stochastic Hybrid Systems Formulation," *Advances in Space Research*, Vol. 69, No. 9, 2022, pp. 3460–3477.
https://doi.org/10.1016/j.asr.2022.02.034

[13] Vendy, B., and Plummer, D., "Autonomous Stationkeeping of Geostationary Satellites," *IFAC Proceedings*, Vol. 12, No. 4, 1979, pp. 95–100.
https://doi.org/10.1016/S1474-6670(17)65721-5

[14] Ray, S., "A Quick Review of Machine Learning Algorithms," *International Conference on Machine Learning, Big Data, Cloud and Parallel Computing (COMITCon)*, Inst. of Electrical and Electronics Engineers, Piscataway, NJ, 2019, pp. 35–39.
https://doi.org/10.1109/COMITCon.2019.8862451

[15] Jain, A., Mao, J., and Mohiuddin, K., "Artificial Neural Networks: A Tutorial," *Computer*, Vol. 29, No. 3, 1996, pp. 31–44.
https://doi.org/10.1109/2.485891

[16] DiBona, P., Foster, J., Falcone, A., and Czajkowski, M., "Machine Learning for RSO Maneuver Classification and Orbital Pattern Prediction," *Advanced Maui Optical and Space Surveillance Technologies Conference*, Maui Economic Development Board, Kihei, Hawaii, 2019.

[17] Cipollone, R., Leonzio, I., Calabrò, G., and Di Lizia, P., "An LSTM-Based Maneuver Detection Algorithm from Satellites Pattern of Life," *2023 IEEE 10th International Workshop on Metrology for AeroSpace (MetroAeroSpace)*, IEEE Publ., Piscataway, NJ, 2023, pp. 78–83.
https://doi.org/10.1109/MetroAeroSpace57412.2023.10189993

[18] Khatri, Y., and Scheeres, D., "Nonlinear Semi-Analytical Uncertainty Propagation for Conjunction Analysis," *Proceedings of 72nd International Astronautical Congress, International Astronautical Federation*, IAC-21, C1,3,12,x64896, Paris, France, 2021.

[19] Hall, Z., Singla, P., and Johnson, K., "Reachability-Based Search for Tracking of Noncooperative Maneuvering Satellites in Data Sparse Environment," *Journal of the Astronautical Sciences*, Vol. 70, No. 2, 2023, pp. 1708–1734.
https://doi.org/10.1007/s40295-023-00365-z

[20] Zhou, X., Qiao, D., and Macdonald, M., "Orbit Determination for Impulsively Maneuvering Spacecraft Using Modified State Transition Tensor," *Journal of Guidance, Control, and Dynamics*, Vol. 47, No. 5, 2024, pp. 1–18.
https://doi.org/10.2514/1.G007814

[21] Blackman, S., and Populi, R., *Design and Analysis of Modern Tracking Systems*, Artech House, Boston, MA, 1999, Chap. 6.

[22] Serra, R., Yanez, C., and Frueh, C., "Tracklet-to-Orbit Association for Maneuvering Space Objects Using Optimal Control Theory," *Acta Astronautica*, Vol. 181, April 2021, pp. 271–281.
https://doi.org/10.1016/j.actaastro.2021.01.026

[23] Kerr, E., Falco, G., Maric, N., Petit, D., Talon, P., Petersen, E. G., Dorn, C., Eves, S., Sánchez-Ortiz, N., Gonzalez, R. D., et al., "Light Curves for GEO Object Characterisation," *8th European Conference on Space Debris*, ESA Space Debris Office, Darmstadt, Germany, 2021, pp. 9–20.

[24] Vasile, M., Walker, L., Campbell, A., Marto, S., Murray, P., Marshall, S., and Savitski, V., "Space Object Identification and Classification from Hyperspectral Material Analysis," *Scientific Reports*, Vol. 14, No. 1, 2024.
https://doi.org/10.1038/s41598-024-51659-7

[25] Bertolini, C., Cipollone, R., De Vittori, A., Di Lizia, P., and Massari, M., "Space Object Identification and Correlation Through AI-Aided Light Curve Feature Extraction," *Aeronautics and Astronautics AIDAA XXVII*, Materials Research Proceedings, Millersville, PA, 2023, pp. 499–503.
https://doi.org/10.21741/9781644902813-109

[26] Shuster, M. D., "Uniform Attitude Probability Distributions," *Journal of the Astronautical Sciences*, Vol. 51, No. 4, 1996, pp. 451–475.
https://doi.org/10.1007/BF03546294

[27] Markley, F. L., and Crassidis, J. L., *Fundamentals of Spacecraft Attitude Determination and Control*, Springer, New York, 2014, pp. 383–388.
https://doi.org/10.1007/978-1-4939-0802-8

[28] Battin, R., *An Introduction to the Mathematics and Methods of Astrodynamics*, AIAA Education Series, AIAA, Reston, VA, 1999, pp. 419–470, Chap. 9.
https://doi.org/10.2514/5.9781600861543.0419.0470

[29] Schaub, H., and Junkins, J. L., *Analytical Mechanics of Space Systems*, AIAA Education Series, AIAA, Reston, VA, 2003, pp. 613–617, Chap.

14.
https://doi.org/10.2514/4.861550

[30] Yamanaka, K., and Ankersen, F., "New State Transition Matrix for Relative Motion on an Arbitrary Elliptical Orbit," *Journal of Guidance, Control, and Dynamics*, Vol. 25, No. 1, 2002, pp. 60–66.
https://doi.org/10.2514/2.4875

[31] Reynolds, R. G., "Direct Solution of the Keplerian State Transition Matrix," *Journal of Guidance, Control, and Dynamics*, Vol. 45, No. 6, 2022, pp. 1162–1165.
https://doi.org/10.2514/1.G006373

[32] Wan, E., and van der Merwe, R., "The Unscented Kalman Filter," *Kalman Filtering and Neural Networks*, edited by S. Haykin, Wiley, New York, 2001, Chap. 7.

[33] Nebelecky, C. K., "New Variations of Multiple Model Adaptive Estimation for Improved Tracking and Identification," Ph.D. Thesis, Univ. at Buffalo, The State Univ. of New York, Amherst, NY, Feb. 2014.

A. Rosengren
Associate Editor